TRABAJO DE FIN DE MÁSTER

Study and characterization of ultra-low background micromegas detectors for their installation and use in IAXO (International AXion Observatory)

Author:
Itxaso Beatriz Antolín Rojo

Supervisor:
Dr. Jaime Ruz Armendariz

UNIVERSIDAD DE ZARAGOZA
Departamento de Física Teórica
Área de Física Atómica, Molecular y Nuclear

July 10, 2024

Acknowledgements

First, I would like to thank Jaime Ruz, my supervisor, not only for his help, patience, and time but also for trusting me throughout the entire process.

I also want thank to María Jimenez for sharing data from the IAXO-Lab and for everything I have learned from her.

To the whole corridor for their willingness to help, especially to Javier Galán, Cristina Margalejo and Luis Obis for their support with REST-related matters, and also to Juan Antonio García, Hector Mirallas, and Juan F. Castel for their dedication in the laboratory.

To all my friends, especially those from my master's and EPFL, for their unconditional support.

And last but no least, I am very grateful to my parents for always being there and motivating me to keep it up.

Contents

List of Figures

List of Tables

Abstract

The nature of dark matter remains one of the most profound mysteries of modern physics. Over the past decades, it has attracted hundreds of physicists from around the world, leading to the proposal of new theories beyond the standard model of particle physics that predict the existence of particles with a wide variety of properties. This has demanded the application of a diverse set of experimental techniques, from underground laboratories to particle accelerators or even space missions, which have succeeded in reducing the parameter space in which the candidates hypothesized as dark matter constituents are postulated to exist.

Experiments that combine the use of X-ray optics and state-of-the-art ultra-low background detectors, such as the International Axion Observatory (IAXO) that will be built at the German Electron Synchrotron (DESY), are key to discover one of the ultralight bosonic dark matter candidates: the axion.

This work is motivated by the need for highly efficient detectors in experiments such as IAXO to enhance axion detection. In particular the challenging the axion-nucleon coupling. For this purpose, a range of simulations have been performed with the goals of studying the intrinsic efficiency of the IAXO-D1 prototype. The use of an Argon + 1% isobutane gas mixture has been investigated at different pressures and the detector response for different axion spectra has been obtained. To fulfill this task, a new code based on the REST (Rare Event Searches Toolkit) software in combination with the Geant4 simulation toolkit has been used. The results of the simulations have been analyzed, leading to the conclusion that the combination of a Micromegas readout with a 6 cm drift chamber significantly enhances nominal performance of the proposed IAXO's baseline detector, especially in the case of the study of the axion-nucleon coupling. All the results obtained with the new proposed drift geometry have been compared with those obtained for the IAXO-D1 prototype.

1. Introduction

Dark matter (DM), an elusive and invisible component of the universe, is primarily inferred through its gravitational effect on visible matter. It cannot be observed directly because it neither emits, absorbs, nor interacts with electromagnetic radiation. Yet, its existence is inferred from its gravitational effects on visible matter in the universe, such as galaxy rotation curves and galaxy clusters [1] and the measured Cosmic Microwave Background [2]. While the exact percentage of dark matter in the universe is unknown, it is estimated to make up approximately 27% of the universe's total mass and energy content. This value is based on the most widely accepted model of the universe's composition, the ΛCDM model [3].

Currently, some of the most compelling candidates for dark matter constituents are Weakly Interacting Massive Particles (WIMPs), which are hypothetical non-relativistic particles that are electrically neutral and interact through gravity and with W and Z bosons of the SM [4]; super symmetric particles such as the neutralino or the gravitino [5], theorized to be stable and electrically neutral; Primordial Black Holes, which are supposed to have been formed in the early universe [6]; and axions, ultra-light particles that interact very weakly with standard model particles, predicted to have properties that make them suitable candidates for cold dark matter [7].

The axion is a hypothetical elementary pseudo-scalar particle that was originally postulated to address the strong CP problem: in QCD (quantum chromodynamics), the strong CP problem arises because the theory allows for a dimensionless term known as the θ-term, which would introduce CP-violation. However, experimental evidences disagree with the theoretical prediction, since they suggest that CP-violation in strong interactions is extremely small, close to zero.

In order to solve this problem, the Peccei-Quinn mechanism was proposed by Roberto Peccei and Helen Quinn in the late 1970s [8, 9]. It introduces a new scalar field called the axion field, which dynamically adjusts its value to minimize the θ-term in the QCD Lagrangian, effectively solving the strong CP problem and therefore, explaining the observed absence of strong CP-violation. Besides, it is well known that the Peccei-Quinn mechanism has implications for dark matter, due to the fact that axions are extremely light, neutral particles.

Axions and similar particles, like the more generic pseudo-scalar bosonic Axion Like Particles (ALPs), can have a wide range of possible masses and coupling strengths, leading to a large parameter space that will be explored by experiments such as the International Axion Observatory (IAXO). It is a fourth generation axion helioscope based on improving the magnetic field volume, X-ray focusing optics and detector technology of the current state-of-the-art helioscope, CAST (CERN Axion Solar Telescope) experiment [10] that started operating in 2003 and finished its data taking in 2021 at CERN (European Organization for Nuclear Research). As a previous step to IAXO, BabyIAXO will be a scaled-down prototype that will facilitate the examination of further enhancements. Both, IAXO and BabyIAXO are programmed to

be set up at DESY (Deutsches Elektronen-Synchrotron) in Hamburg, Germany. IAXO makes use of an strong magnetic field volume produced by a superconducting magnet with toroidal geometry. Solar axions entering the magnetic field region are expected to be converted into X-ray photons through the inverse Primakoff effect. These photons would then be focused by dedicated X-ray telescopes and detected by intrinsically radiopure X-ray detectors: ultra-low background Microbulk Micromegas such as the IAXO-D1 prototype that is being characterized at the IAXOLab in Zaragoza.

2. Axions and the Strong CP Problem

QCD is the non-abelian gauge field theory that describes the strong interactions between quarks mediated by gluons. Its Lagrangian is given by the following expression:

$$\mathcal{L}_{QCD} = \sum_f \bar{q}_f \left(i\gamma^\mu D_\mu - m_f\right) q_f - \frac{1}{4} G^a_{\mu\nu} G^{\mu\nu}_a - \bar{\theta}\frac{\alpha_s}{8\pi} G^a_{\mu\nu}\tilde{G}^{\mu\nu}_a. \tag{1}$$

where q_f represents the quark field with flavour f; γ^μ is the Dirac matrix; m_f is the quark mass; D_μ is the covariant derivative; α_s is the strong coupling constant; $\bar{\theta} \in (0, 2\pi)$ is the θ-parameter; $G^a_{\mu\nu}$ is the gluon field strength tensor where a is the color index that goes from 1 to 8; and $\tilde{G}^{\mu\nu}_a = \frac{1}{2}\epsilon^{\mu\nu\alpha\beta} G_{a\alpha\beta}$ is its dual. In Eq. 1, the first term describes the kinetic and mass terms for quarks, the second one the gluon self-interactions and the last one is a non-perturbative contribution called the θ-term, which is the only one that violates the CP symmetry. However, as mentioned in the introduction, CP violation has never been detected experimentally.

The presence of the θ-term induces a permanent electric dipole moment (EDM) for neutrons, but the most sensitive measurements of the neutron EDM to date [11, 12] set an experimental limit of $|d_n| < 1.8{\cdot}10^{-26}\ e{\cdot}cm$ at a 90% of confidence level (C.L.), which implies that $|\bar{\theta}| < 10^{-10}$. Since $\bar{\theta}$ is a parameter that can take any value between 0 and 2π in the theory [1, 13], this presents a disagreement known as the "naturalness" problem for the SM[1], resulting in a fine-tuning known as the strong CP problem.

2.1. A solution: the axion

In 1977, Roberto Peccei and Helen Quinn postulated what is considered the most elegant solution to the strong CP problem: the Peccei–Quinn mechanism [8, 9]. It is based on the introduction of a new global, chiral $U(1)$ symmetry known as the Peccei-Quinn symmetry, $U(1)_{PQ}$, that is spontaneously broken at some large energy scale denoted as f_a. An inevitable consequence of the $U(1)_{PQ}$ symmetry breaking is the existence of a new neutral particle, the axion, which is the Nambu-Goldstone boson of the broken symmetry. At energies below f_a (still PQ scale), the coupling of the axion to gluons occurs, and in the low temperature limit[2],

[1] The SM predicts a neutron EDM of $|d_n| \sim 10^{-16}\ e \cdot cm$, considering $\bar{\theta} \sim 1$.

[2] Where the temperature is significantly below the QCD phase transition temperature (~ 200 MeV).

the axion mass is generated via explicit breaking of the chiral symmetry due to the mixing with pions[3] which means that the axion is, more accurately, a light pseudo Nambu-Goldstone boson [1]. Thus, it is the QCD axion interaction with the gluon that achieves the PQ solution, by promoting the θ-term to a dynamical variable equal to a/f_a, that relaxes to zero in a natural way.

2.2. Axion properties

The phenomenological properties of the axion, apart from being determined by the PQ symmetry breaking scale f_a, are closely related to those of the neutral pion, π^0. To be specific, the most relevant parameters for axion searches are the axion mass and its interactions strengths.

As axions can mix with pions, they can acquire mass depending on the pion mass, $m_\pi = 135\,\mathrm{MeV}$, and decay constant, $\mathrm{f}_\pi \simeq 92\,\mathrm{MeV}$. It is quantified as follows:

$$m_a = \frac{\sqrt{z}}{1+z}\frac{f_\pi m_\pi}{f_a} = 6eV\frac{10^6 GeV}{f_a}, \tag{2}$$

where $z \equiv m_u/m_d$ is assumed for the mass ratio of the up and down quarks [14, 15].

Despite the fact that they are a compelling candidate for the cold dark matter of the Universe, unsuccessful experimental searches and astrophysical constraints suggest that axions must be extremely light and exhibit very weak interactions. Moreover, the axion couplings to ordinary matter particles, such as photons, nucleons and electrons, are inversely proportional to f_a, but they also include significant uncertainties stemming from certain model-dependent numerical parameters [14].

Most of the experiments searching for axions are based on the generic axion coupling to two photons, described by the Lagrangian term,

$$\mathcal{L}_{a\gamma\gamma} = -\frac{C_\gamma \alpha}{8\pi f_a} F_{\mu\nu}\tilde{F}^{\mu\nu} a \equiv -\frac{g_{a\gamma}}{4} F_{\mu\nu}\tilde{F}^{\mu\nu} a = g_{a\gamma}\mathbf{E}\cdot\mathbf{B}a, \tag{3}$$

where $\alpha \sim 1/137$ is the fine structure constant, $F_{\mu\nu}$ and $\tilde{F}^{\mu\nu}$ are the electromagnetic field tensor and its dual, and a is the axion field. C_γ is a dimensionless model dependent parameter given by $C_\gamma \simeq E/N - 2(4m_d + m_u)/3(m_u + m_d) \simeq E/N - 1.92$, where E/N is the model-dependent ratio of the electromagnetic and color anomaly factors. In the KSVZ model the QCD anomaly is induced by heavy exotic coloured fermions so that $\mathrm{E/N} = 0$, and for the DFSZ model, in which axion couples to the SM sector at tree-level through the Higgs portal, the SM quarks and leptons charges imply either $\mathrm{E/N} = 8/3$ or $2/3$ [16]. The axion–photon coupling strength is described by

$$g_{a\gamma} = \frac{\alpha}{2\pi f_a}\left(\frac{E}{N} - \frac{2}{3}\cdot\frac{4+z+w}{1+z+w}\right). \tag{4}$$

[3]The axion-pion mixing arises from the axion-gluon coupling, since the axion and pion are bosons with the same quantum numbers.

Here, $w \equiv m_u/m_s << z$, where m_u is the up quark mass and m_s is the strange quark mass. The most common values in the axion literature for the quark-mass ratios are $z = 0.56$ and $w = 0.028$ [17], although they can be given different values within some limits. Nevertheless, the ratio E/N is the parameter that introduces the largest uncertainty in Eq. 4. Additionally, $g_{a\gamma}$ can be written in terms of the axion mass as

$$g_{a\gamma} = \frac{\alpha}{2\pi}\left(\frac{E}{N} - \frac{2}{3}\cdot\frac{4+z}{1+z}\right)\frac{1+z}{\sqrt{z}}\frac{m_a}{m_\pi f_\pi}, \tag{5}$$

which shows a linear relationship between the axion-photon coupling and the axion mass. In the $g_{a\gamma} - m_a$ parameter space of a given axion model, Eq. 5 fixes what is called the "axion-line".

The axion-photon coupling described above rules the well-known Primakoff effect, based on the fact that photons can oscillate into axions and vice versa (analogous to neutrino oscillations). This plays a significant role in experimental approaches to detect axions, since most of the experiments for axion detection relay on their coupling to virtual photons of a transverse magnetic field and their oscillation back to photons via the inverse-Primakoff process.

2.3. Solar axions

An axion production mechanism is the conversion of thermal photons in the solar interior. These photons are converted into axions due to the electric fields of the charged particles in the hot plasma $\gamma + (e^-, Ze) \rightarrow a + (e^-, Ze)$ [18]. Fig. 1 illustrates the generation of axions in the solar core (left) and possible conversion back into photons in the presence of a magnetic field on Earth (right).

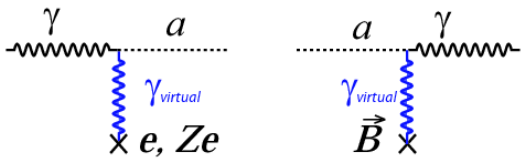

Figure 1: Left: The Primakoff effect, assumed to occur the hot solar core via the $a - \gamma\gamma$ vertex. Right: the inverse process in an external magnetic field that converts the 'invisible' axion to an observable photon [19].

The solar axion emission rate produced by the usual Primakoff effect can be calculated from the spectrum of $\mathbf{E}\cdot\mathbf{B}$ fluctuations, where $\mathbf{E}$ comes from the charged particles forming the plasma and $\mathbf{B}$ is generated by the propagation of thermal photons. Furthermore, it is essential to take into account the fact that particles within the plasma are screened beyond a certain distance, and also that all particles in the Sun are non-relativistic, which means that $\mathbf{B}$ fields originated from moving electric charges are small, making the electro-Primakoff process[4] much less relevant than the ordinary one.

[4]A subdominant axion-production process in which the axion is produced from two virtual photons, both provided by a charged particle.

Considering the modern solar model in [15], the solar axion flux spectrum is computed as:

$$\frac{d\phi_a}{dE} = 6.02 \cdot 10^{10} cm^{-2} s^{-1} keV^{-1} g_{10}^2 E^{2.481} e^{-E/1.205}, \tag{6}$$

where $g_{10} = g_{a\gamma}/10^{-10}\,\mathrm{GeV}^{-1}$ and E is the axion energy in keV. The distribution has its maximum value at 3 keV, its mean energy is 4.2 keV and it vanishes above 10 keV. This is shown in Fig. 2 (right) with respect to the axion energy for $g_{a\gamma} = 10^{-10}$ GeV^{-1} for different values of the dimensionless radial coordinate $r = R/R_\odot$, where $R \in [0, R_\odot]$, together with a contour plot of the solar surface luminosity in axions $\varphi_a(E, r)$ (left).

Nonetheless, there could also exist another hadronic axion emission mechanism from the Sun independent of the axion-photon coupling: the 14.4 keV line from the de-excitation of ^{57}Fe nuclei ($^{57}\mathrm{Fe}^* \rightarrow {}^{57}\mathrm{Fe} + \mathrm{a}$). It stems from the axion-nucleon coupling, which is a consequence of the tree-level coupling of the axion to up and down quarks, and also of an additional contribution owing to the axion-pion mixing. The effective Lagrangian of the axion-nucleon interaction is given by [14]

$$\mathcal{L}_{aN} = i\, a\, \bar{\psi}_N \gamma_5 (g_{aN}^0 + g_{aN}^3 \tau^3) \psi_N, \tag{7}$$

where a is the axion field, $\psi_N = \binom{p}{n}$ is the nucleon doublet, τ^3 is the Pauli matrix, and g_{aN}^0 and g_{aN}^3 are the model-dependent iso-scalar and iso-vector axion-nucleon coupling constants, respectively, which, in the context of hadronic axion models, are proportional to m_N/f_a.

The decay process from the 14.4 keV first excited state to the ground state in the ^{57}Fe nucleus through axion emission, also known as M1 nuclear transition of ^{57}Fe nuclei, is noteworthy. This is due to the fact that the excitation energy to its first excited state is comparable to the

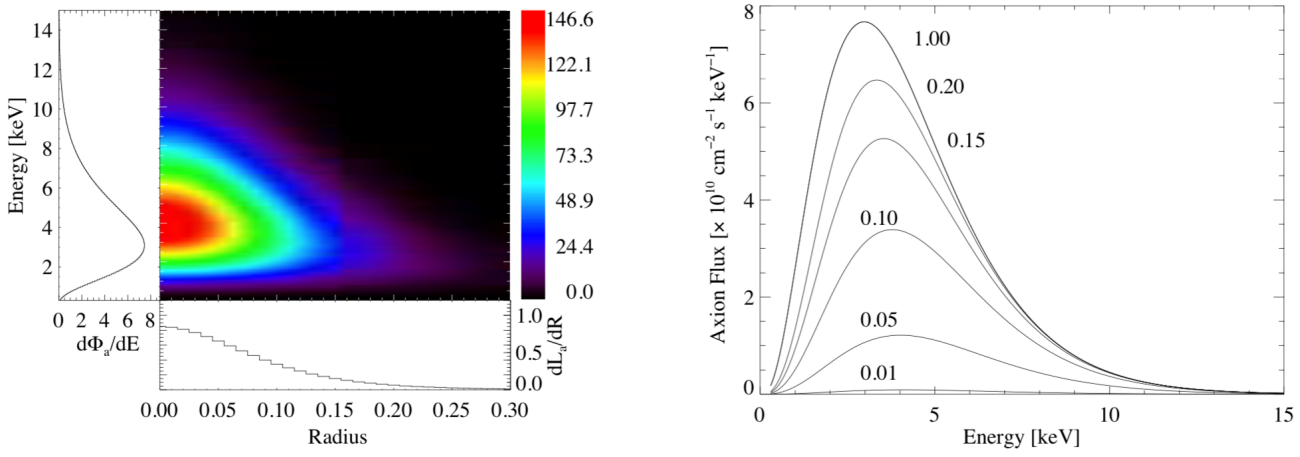

Figure 2: Left: Surface luminosity of solar axions as a function of energy and the radius r on the solar disk, and given in units of axions cm^{-2} s^{-1} keV^{-1} per unit surface area on the solar disc. The radial distribution of the axion energy loss rate of the Sun (dL_a/dR) and the energy distribution of the solar axion flux ($d\Phi_a/dE$) are also shown. Right: differential spectrum of solar axions, derived by integrating the model shown on the left for different values of r in units of the solar radius $R_\odot$. The peak of the spectrum shifts towards lower energies if the integration radius moves towards the solar disc [15].

temperature of the Sun's core ($kT \sim 1.3\,\mathrm{keV}$), implying that it can be thermally excited within the Sun. In [14], the flux of the monoenergetic solar axions produced via this process was computed, resulting in the estimation:

$$\Phi_a = 4.56x10^{23} \left(g_{aN}^{eff}\right)^2 \; cm^2 s^{-1}, \tag{8}$$

where $g_{aN}^{eff} = (-1.19\, g_{aN}^0 + g_{aN}^3)$ is considered a free unknown parameter that characterizes the axion-nucleon coupling.

Appart from hadronic axion models, there are other mechanisms for axion emission from the Sun. For instance, the non-hadronic models, which allow for axion-electron coupling at tree-level via g_{ae}, leading to larger axion fluxes from stars than the traditionally studied Primakoff emission. In non-hadronic axions, the primary emission processes are electron-nucleus bremsstrahlung ($e+Ze \to Ze+e+a$), electron-electron bremsstrahlung ($e+e \to e+e+a$), and Compton-like scattering ($\gamma+e \to e+a$). Additionally, axio-deexcitation and axio-recombination processes play a subdominant role [20]. A detailed representation of each contribution is depicted in Fig. 3.

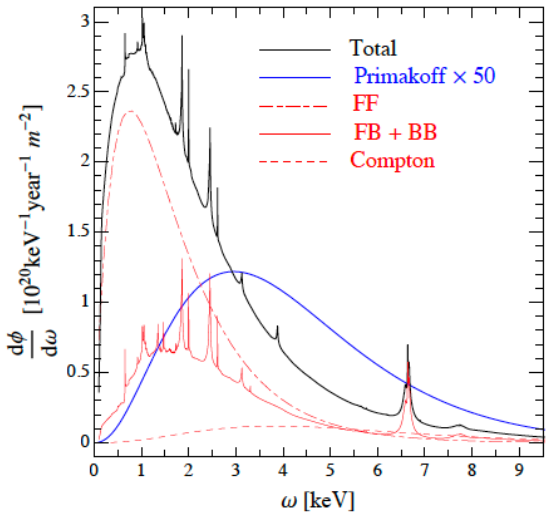

Figure 3: Solar axion flux on Earth for a typical DFSZ model with interaction strength to photons $g_{a\gamma} = 10^{-12}\,\mathrm{GeV}^{-1}$ and electrons $g_{ae} = 10^{-13}$, corresponding to $f_a = 0.85 \times 10^9\,\mathrm{GeV}$. The blue line corresponds to the Primakoff flux and the red lines show the different components of the BCA flux: FF = free-free (bremsstrahlung), FB = free-bound (axio-recombination), and BB = boundbound (axio-deexcitation). The black line is the total flux (taken from [20]).

2.4. Axions as dark matter candidates

In addition to being suitable candidates for dark matter, axions and Axion-Like Particles (ALPs) find strong support as they emerge as potential explanations in various extensions of the Standard Model (SM). Although they were not originally theorized as dark matter particles, they are non-relativistic neutral particles that interact extremely weakly with ordinary matter and with themselves. This set of properties turn them into potential constituents of the Dark Matter in the Universe [21].

If f_a were small enough, axions could have been formed thermally as a result of the high temperatures in the early stages of the Universe and, in consequence, axions would contribute to the Hot Dark Matter in the Universe. However, Hot dark Matter models are, in principle, discarded by experimental observations.

Otherwise, if the f_a parameter were large, the axion coupling to SM particles would be weak enough, and thus, the thermalization would have not occurred in the early Universe. When the Universe acquired the temperature of the QCD phase transition, the axion potential was generated and then, the axion acquired its mass. The oscillations of the axion field around the CP conserving minimum of its effective potential, the so-called misalignment mechanism, generated a cosmological population of non-relativistic axions that would potentially contribute to Cold Dark Matter. The initial value of the DM axion field before these oscillations started, known as the misalignment angle, is an unknown parameter of this theory.

3. Strategies for axion searches

There are different possible natural sources of axions, such as Supernovae or stars, that offer the opportunity to detect axions from Earth as well as the natural abundance of axions as one of the constituents of DM in the Universe. Nevertheless, it is also worth taking into account purely laboratory experiments, in which man-made sources of axions are used [22, 23]. All these experiments mostly rely on the $g_{a\gamma}$ coupling via the (inverse) Primakoff effect, and the most remarkable ones can be divided into three types.

To begin with, 'haloscopes' are resonant cavities designed to detect axions from the dark matter galactic halo as they become immersed in a strong magnetic field during their travel through Earth[24]. Their working principle is based on an electromagnetic resonator whose frequency is matched for a given axion mass. If this happens, an enhancement of the axion to photon conversion rate through the inverse Primakoff process is possible. However, due to the fact that the axion mass is unknown, the frequency of the resonator needs to be continuously tuned, covering a certain range of frequencies corresponding to different axion masses. It is important to keep in mind that the sensitivity of these experiments is subject to the local DM density on Earth, which is an unknown parameter. Examples of these experiments are ADMX (Axion Dark Matter eXperiment) [25] and HAYSTACK (The Haloscope At Yale Sensitive To Axion CDM) [26], which use solenoids to produce the magnetic fields.

A different approach for axion detection is the 'LSW' technique, that uses lasers together with strong dipole magnets to probe the coupling between photons and axions in a magnetic field [1]. One of the advantages of this type of experiments is that the origin of their systematic uncertainty is only experimental, since they do not rely on model-dependent astrophysical or cosmological sources of axions. LSW setups consist of a high-power laser traversing a magnetic field, with a beam pointing to a wall that blocks the light. The interaction of the laser with the magnetic field can produce a beam of axions able to cross the wall. On the opposite side

of the wall, there is a second independent magnetic field which converts the axions back into photons that can subsequently be detected by a single-photon detection system. ALPS (Axion Like Particle Search) is an example of this kind of experiments, also designed to search for ALPs [22].

To finalise, 'helioscopes' are a type of telescope that search for axions originating from the Sun, the closest astrophysical source to Earth. If axions exist, they would be produced in the core of the Sun. When these solar axions interact with a strong magnetic field on Earth, they can be detected as X-ray photons. The success of such experiments depends on the current understanding of solar physics, which is well-established and determines the axion flux spectrum (such as Eq. 6). A well-known example of helioscopes is CAST [27]. The following sections will provide a detailed introduction and discussion of IAXO, its successor.

4. The International AXion Obsevatory (IAXO)

IAXO is a fourth-generation helioscope whose primary objective is to search for axions and ALPs originating in the Sun. It does this by converting them into detectable X-ray photons through the inverse Primakoff effect within a large cross-sectional transverse magnetic field [28]. Subsequently, X-ray optics concentrate the resulting photons into focal spots that are imaged with small-area detectors to achieve ultra-low background levels (see Fig. 4). By aligning the magnet with the core of the Sun and tracking its movement, an excess of X-rays is expected to be measured compared to background levels when the magnet is not pointing at the Sun [1].

IAXO is expected to be sensitive to the axion-photon coupling $g_{a\gamma}$, as well as to the axion-electron coupling g_{ae} and the axion-nucleon coupling g_{an}, and it has also been designed to include new equipment such as microwave cavities to allow for relic axions searches. Furthermore, it seeks to improve the sensitivity to $g_{a\gamma}$ by over an order of magnitude compared to existing astrophysical and experimental limits which will allow to explore $g_{a\gamma}$ values down to $10^{-12}\,\mathrm{GeV}^{-1}$ for a broad spectrum of axion masses [28]. To achieve this, BabyIAXO will serve as an intermediate experimental stage for IAXO, to test all IAXO's subsystems[5] in advance of the full size experiment. IAXO's sensitivity to solar axions (or ALPs) will reach $g_{a\gamma} \sim 1.5 \cdot 10^{-11}\,\mathrm{GeV}^{-1}$, and masses up to $m_a \lesssim 0.25\,\mathrm{eV}$ [28].

The data collection of IAXO will be divided into two campaigns, named Run-I and Run-II, each assumed to last for 3 years. During the first data collection phase, Run-I, magnet bores will be in vacuum[6] to determine the sensitivity of the experiment for m_a below $0.01\,\mathrm{eV}$. In the following phase, Run-II, magnet bores will be filled with ^{4}He buffer gas, with its density adjusted from 0 to 1 bar at room temperature. This phase aims to enhance the sensitivity in the high mass range, reaching up to $m_a \lesssim 0.25\,\mathrm{eV}$, and exploring the DFSZ axion models [28].

[5] That is to say, magnet, optics and detector. To maximize the figure of merit (FOM) of the helioscope, a global optimization for the FOM of these components, along with that of the exposure time, is required.

[6] This is the situation replicated in the simulations of this work.

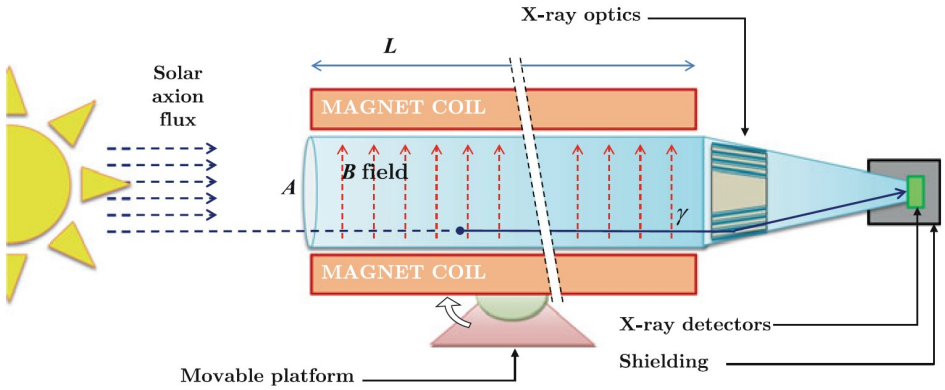

Figure 4: Conceptual design of the IAXO helioscope. Axions originating from the Sun undergo conversion within the transverse magnetic field produced by a large magnet coil. Afterwards, an X-ray telescope focuses these photons into a focal where a low-background detector captures images of the photons (taken from [28]).

IAXO is also expected to be able to detect the so called ABC solar axion flux[7]. Therefore, it will also be sensitive to non-hadronic axions with an axion-electron coupling of $g_{ae} \sim 10^{-13}$. In this scenario, the axion signal depends on the product $g_{ae} \cdot g_{a\gamma}$, where g_{ae} represents the electron coupling responsible for axion production in the Sun, and $g_{a\gamma}$ governs axion conversion within the magnetic field of the helioscope. Consequently, IAXO could have the potential to achieve sensitivity surpassing the current stringent astrophysical limit on g_{ae} for the first time in an experiment (see [28] for more details on the g_{ae} limit). Additionally, IAXO will also be sensitive to the axion emission from the ^{57}Fe M1 transition in the Sun and, analogously, it will depend on the $g_{aN} \cdot g_{a\gamma}$ product.

In the same way as for IAXO, the data collection of BabyIAXO stage will consist of two phases: the first one in vacuum and the second one with buffer gas, each expected to last 1.5 years of effective exposure. The gas phase will also be distributed in various density steps to adjust the sensitivity to the KSVZ axion model $g_{a\gamma}$ for a wide mass range [28].

As in the case of IAXO, both BabyIAXO magnet bores will be equipped with two detection lines, each one composed by an X-ray telescope and ultra-low background detector [28]. BabyIAXO's strength resides in the fact that it will already be sensitive to unexplored axion parameter space regions.

4.1. The baseline Micromegas detector: IAXO-D1

BabyIAXO will feature two low-background pixelated X-ray detectors at the focal planes of its X-ray optics. The technology of these detectors will consist of small gaseous Time Projection Chambers[8] (TPC), approximately 6 cm wide and 3 cm drift, with pixelated readouts of micro-mesh gaseous structures manufactured using the microbulk technique [30, 31], microbulk

[7]Originating from (electron-ion and electron-electron) axion-Bremsstrahlung, Compton, and axio-deexcitation of ions [20].

[8]See [29] for more information.

Micromegas. The components of these detectors are constructed from highly radio-pure materials and are surrounded by both passive shielding, such as lead, copper and cadmium, and active shielding, which consist of muon vetoes (scintillating plastics), to reduce the influence of cosmic radiation [28]. Combining these techniques with event discrimination strategies based on the detailed topological information of the background events, BabyIAXO's Micromegas detectors are designed to achieve a background of $\sim 10^{-7}\,\mathrm{counts\,keV^{-1}\,cm^{-2}\,s^{-1}}$ or lower, with a threshold of at least 1 keV. These detectors will serve as prototypes for the ones to be installed in the future IAXO.

4.1.1. Detector Design

The IAXO-D1 prototype is similar to the last generation of CAST detectors. It is a compact TPC equipped with a Micromegas readout at the anode, with its cathode facing the magnet bore, allowing signal X-rays to enter the detector. The usual setup of the detector makes use of 1.2 bar of Argon gas, together with a 1 % of quencher (C_4H_{10}, also known as isobutane). The X-rays coming from the magnet location enter the conversion volume through a window made of $\sim 4\mu$m aluminized Mylar foil, which serves as the TPC cathode.

This window is reinforced by a metallic strong-back to withstand the pressure difference relative to the magnet vacuum (or buffer gas) system [28]. Its body and chamber walls are made of 18 mm thick radio-pure copper.

It also has a field shaper to enhance the uniformity of the drift field and minimize border effects. This field shaper is externally covered by a 3 mm thick Teflon[9] layer in order to block copper fluorescence from the detector body.

The readout plane consist of a 2D strip pattern of 120 strips per axis covering a surface of $6 \times 6\,\mathrm{cm^2}$ [28]. Fig. 5 illustrates the basic structure of the detector prototype. In this type of gaseous detector, photons, or charged particles with enough energy passing through the active gas volume, can ionize the atoms or molecules of the gas creating e^- – ion pairs[10]. A uniform electric field is applied by setting a positive and a negative electrode to a potential difference, and this causes the charges to drift within the gas, producing a current at the electrodes. This results in a de-

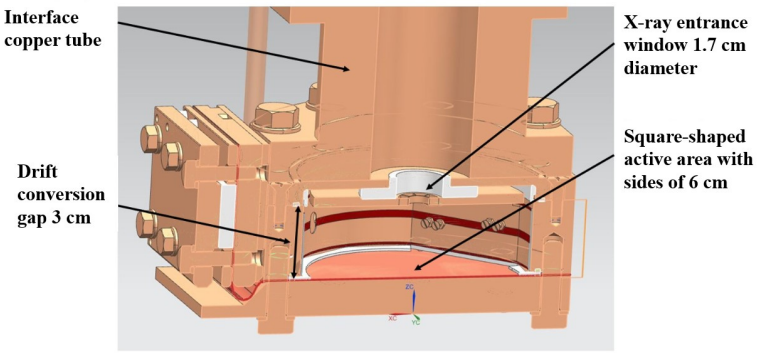

Figure 5: IAXO-D1 detector prototype design (taken from [28]).

[9] Trade name of PTFE (Polytetrafluoroethylene).

[10] The W-value is the energy required to produce a e^- – ion pair for a particular gas. In the case of the Argon, it is $26\,eV$.

tectable signal, that is, in an electric pulse that can be measured by a readout placed at one of the electrodes and recorded by acquisition electronics.

Photons mainly interact through three processes: at low energies, the dominant process is the photoelectric effect. Around 100 keV, Compton scattering becomes dominant, and at approximately 10 MeV, the pair production mechanism starts to be the most important. Since the energy range of interest for this work is between 1 keV and 14.4 keV, the photoelectric effect is the most relevant process.

When the photoelectric effect occurs, the emission of a photoelectron (primary ionization) creates a vacancy in the corresponding atomic shell, and there are two main mechanisms by which an excited atom fills a vacancy, resulting in secondary emissions: the Auger effect and X-ray fluorescence. In the Auger effect, an electron from a higher energy level fills the vacancy. The energy difference between the atomic levels is transferred to another electron within the same atom. If this energy exceeds the binding energy, the electron is ejected into the gaseous detection medium, where it can initiate an ionization process, producing a detectable signal [32]. When fluorescence occurs, a vacancy is filled by an outer shell electron, resulting in the emission of an X-ray photon with energy equal to the difference between the electronic levels. This photon can interact with the gas volume to produce a detectable signal. However, if it escapes from the gas without interacting, it will add an escape peak in the detected energy spectrum at an energy of $E_\gamma - E_{shell}$ [32, 33].

When talking about ionization processes, it is worth mentioning the Fano factor. It is the factor that indicates the magnitude of the fluctuation in the number of primary electrons, since the smaller it is, the smaller the variance of the fluctuation, and it depends of the gas mixture and the electron energy. Indeed, this fluctuation is the first contribution to the energy resolution (ER) of a gaseous detector.

After the photoelectric effect, the emitted primary charges will ionize or excite the atoms of the gas as long as they have sufficient energy. In a gaseous medium, electromagnetic interactions (Coulomb interactions, bremsstrahlung, Cherenkov radiation and transition radiation [33]) are the most probable ones. It is common to use a mixture of a high-Z noble gas (which has a high cross-section for the photoelectric effect and vanishing electron absorption) with a small quantity of a organic molecular gas called "quencher" to ensure that each pulse discharge terminates [34].

Due to the applied electric field, the electrons accelerate towards the anode, where the detector readout is located, while the ions move towards the cathode (showcased in Fig. 6). During their drift, electrons are considered to move at a constant velocity because the acceleration from the electric field is balanced by collisions with gas atoms, which slow them down. What is more, the drift velocity of the electrons depends on the scattering cross-section of the target gas [32]. Quencher gases are used in order to improve the drift velocity[11] of noble gases: in this work an Argon gas mixture with a 1 % of C_4H_{10} (isobutane) is used.

[11] Or, in other words, relatively high energy loss for the electron.

As the electrons drift within the electric field, they can deviate from their desired trajectory due to collisions with gas particles. This is known as diffusion, and it can affect the topological information of the gaseous detector. Nevertheless, quenchers can also be used to reduce this phenomenon.

There are two main processes that reduce the number of the electrons produced by the primary emission and therefore affect the final charge of the event: recombination and attachment. The first occurs when the drifting electrons encounter positive ions moving in the opposite direction, while the second refers to the absorption of electrons by impurities in the gas, such as air and water. However, it can be reduced by minimizing the leaks of the gas system as well as by using a continuous flow of clean gas.

Under a sufficiently strong electric field ($\sim \mathrm{kV\,cm^{-1}}$), a chain reaction of $e^- -$ ion pairs production known as electron avalanche is triggered. High electric field amplification regions are employed in gaseous detectors to amplify the single electron charges formed in the ionization region, enabling them to produce a detectable signal[12]. The number of final electrons after the avalanche can affect the energy resolution of the detector, not only due to statistical reasons, but also due to attachment, electronic noise, geometrical imperfections and more parameters. Once the $e^- -$ ion pairs are generated in the amplification region, they will drift towards the corresponding electrodes. This movement of charges within the electric field generates a current in the electrodes, that is, a measurable signal. The current induced in an electrode depends on the velocity of the charge and as electrons are approximately 10^3 times faster than ions, the signals they induce will have different characteristic times [32].

4.1.2. Detector Readout Plane

A Micromegas consists of two parallel electrodes separated by an amplification space of about $35 - 100\mu$m for charge multiplication. The cathode is made of a thin copper micromesh, while the anode consists of copper strips that form the readout plane. In this type of Micromegas a pixel is referred to as the crossing between each orthogonal strip [32]. IAXO-D1's readout is a square of 60 mm sides, with a total of 120 strips per axis separated by a pitch of $500\,\mu$m. IAXO-D1 prototype works as a TPC detector where the Micromegas readout plane plays the role of a segmented anode, with the cathode of the drift chamber positioned parallel to the Micromegas mesh. As electrons are released within the gas chamber after ionization occurs, they drift towards the mesh and enter the amplification gap following the electric field lines. Within this gap, an avalanche occurs, leading to the generation of a large number of $e^- -$ ion pairs that induce signals on the anode and on the cathode mesh respectively (see Fig. 6).

In Fig. 7, a Gaussian fit over a quadratic background has been performed in order to calculate the detector resolution at 5.9 keV for a recent calibration in the IAXO-Lab. The

[12]This is accompanied by the fact that the electrons in the amplification region can alter the electric field, causing multiplication to saturate, a phenomenon commonly referred to as a spark.

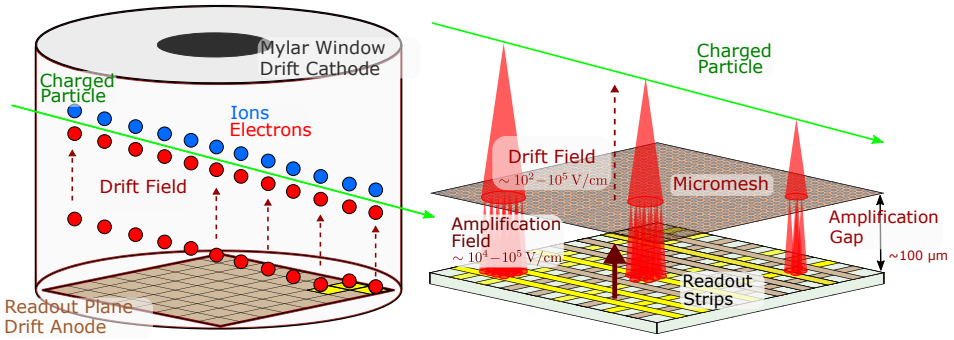

Figure 6: Left: diagram of IAXO-D1's TPC. Right: detection principle of a Micromegas detector. Electrons generated by ionization move towards the readout plane due to the electric field in the drift area of the chamber. Right after reaching the Micromegas mesh, the charges enter the amplification region, inducing a signal on the readout strips. This signal is then used to reconstruct the energy and position of the event in the readout plane (taken from [35]).

topology of the signals detected by the readout plane are unequivocal of the nature of the events registered in the drift chamber of the detector. For instance, X-ray track events share symmetry in the X-Y readout plane (Fig. 7 Right), and have an specific number of hits per event that depends on the energy of the incident X-ray (Fig. 7 Left).

4.2. Intrinsic efficiency of IAXO-D1

The work performed for this master's thesis has developed novel code [36] to obtain the intrinsic efficiency of the IAXO-D1 and what it could be a natural extension of the current prototype to enhance the detector sensitivity for axion searches. In particular, for the case of

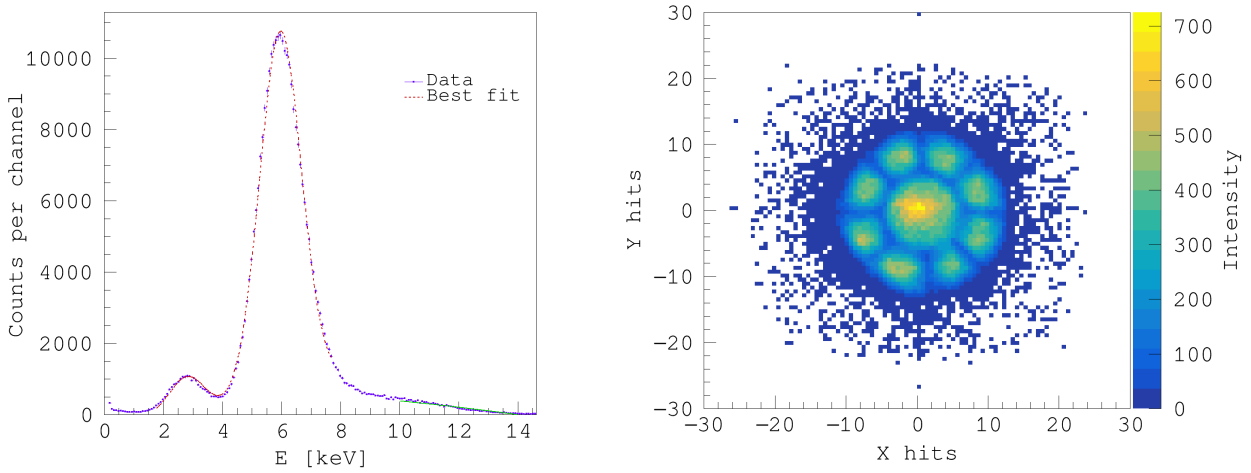

Figure 7: Left: calibration spectrum taken in the IAXO-Lab using a ^{55}Fe source showing an energy resolution of $\sim$ 30% with a binning of 0.075 keV/channel (channel = energy bin). Right: hit map (scatter plot) of the corresponding calibration data taking on the readout plane.

axion-nucleon coupling.

This section presents the simulations carried out using RestG4, a REST-based code that makes use of the generic Geant4[13] library to define contour conditions, execute, and collect the simulated results in the form of ROOT files encapsulated as REST C++ objects. The RestG4 process requires only of two inputs: an RML configuration file specifying the simulation conditions and a GDML file defining the detector's geometry.

The number of events to be simulated and the detector geometry are defined in the RML file. To calculate the intrinsic efficiency[14] at a given energy, individual simulations have been performed in the 0-to-16 keV energy range of interest with a ΔE interval of 0.25 keV. Each simulation has been set to register $10,000$ events in the detector such that the statistical uncertainty of the simulation is consistent with each other[15]. The geometry of IAXO-D1 detector described in the GDML file follows IAXO's repository instructions[16] (see Fig. 8). For the proposed extended version of 6 cm drift distance, the original GDML file has been consequently adapted, by extending the drift distance of the original one.

The RML file defines the primary particle generator, which is used to define the spatial origin of the sources, the type of particles to launch, as well as their energy, angular distribution, and other functions that can be added to describe a wide range of physics scenarios.

In this work, the events have been generated from a single point close to the chamber and in front of the Mylar window, centered with respect to it, within a vacuum environment.

The primary particles are photons with a mono-energetic energy distribution. In the following section a scan over the different axion emission spectra is performed to take into consideration the actual nature of the source.

The detector volume has been filled with Ar + 1% C_4H_{10}, as mentioned in previous sections. The information stored in the ROOT file identifies the gas volume in the GDML geometry as the sensitive volume for data storage[17].

The results of these simulations are illustrated in Fig. 9, where the efficiency plots are shown for different pressure values: 1.2 bar, which is a typical configuration used for data takings; 1.6 bar, an intermediate value;

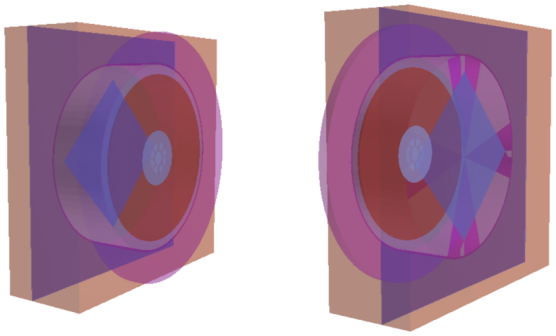

Figure 8: Overview of the geometry of the 3 cm drift distance chamber used in the simulations.

[13]Toolkit for creating simulations of the interaction of particles or radiation with matter using Monte Carlo methods (geant4.web.cern.ch). All the processes explained in chapter 4 are implemented in Geant4.

[14]Referred to the efficiency of IAXO-D1's TPC excluding the detector's interface copper tube and shielding.

[15]This implies that the total number of events simulated is one or even three orders of magnitude larger, depending on the whole set of conditions applied.

[16]Taken from IAXO's repository: github.com/iaxo.

[17]If an event does not produce an energy deposit (or hit) in the sensitive volume, the event will not be stored.

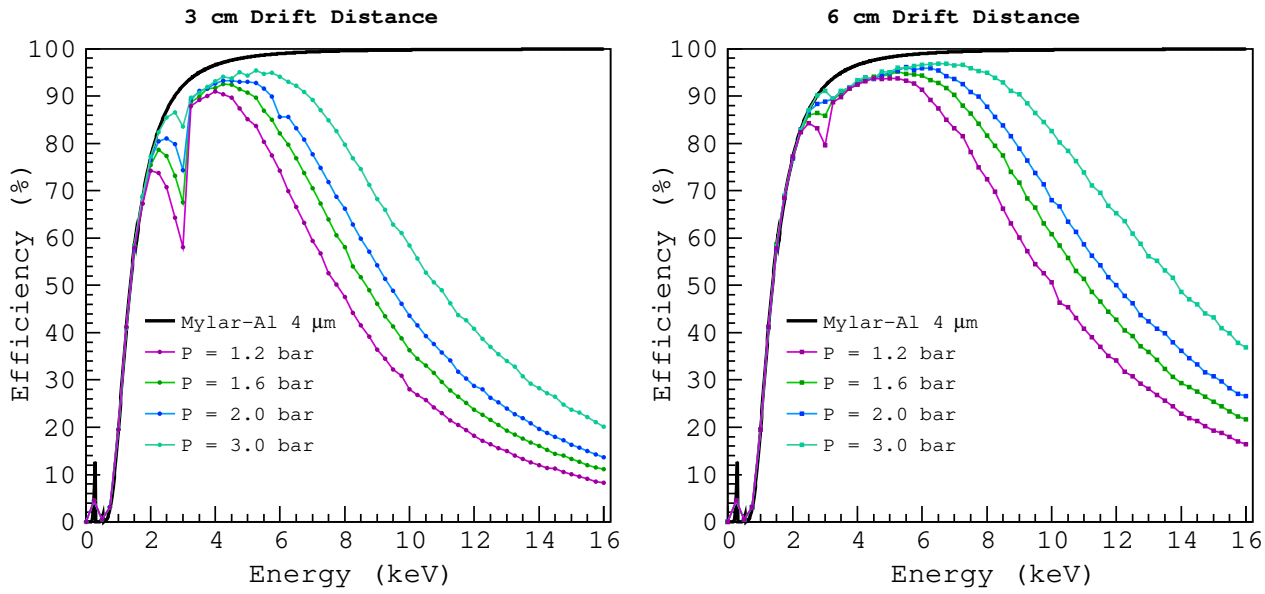

Figure 9: Intrinsic efficiency of the detector in % at different pressures for a 3 cm drift distance chamber (left) and a 6 cm drift distance chamber (right). In both plots the photon transmission across the aluminized Mylar window is shown, calculated using CXRO database for X-Ray interactions with matter [38].

2.0 bar, the maximum pressure difference that the current Mylar window design can withstand; and 3.0 bar, to demonstrate how the detector would perform under higher gas density values, provided a new design of the cathode window could withstand such pressure.

Cuts on the deposited energy have also been applied to discard hits with energy lower than that of the primary particles, effectively excluding contributions from secondary excitations.

Fig. 9 clearly shows that the detector's efficiency improves when the size of the chamber is doubled and when pressure is increased, especially at high energies above 4 keV and for the Argon escape peak[18], which is around 3 keV and disappears at 2.0 bar. Additionally, as deduced from Fig. 9, the peak around 0.25 keV is due to the transmittance peak of the 4 μm aluminized Mylar window[19]. Furthermore, by comparing the transmittance plot and the efficiency curves, it can be noted that it is not the gas, but the aluminized Mylar window, the one that determines the energy threshold of IAXO-D1 and its proposed enhancement.

Fig. 10 shows how the efficiency of different selected energies evolve as function of pressure for the IAXO-D1 prototype and the proposed new detector geometry.

4.2.1. Axion spectra convolution

In this section, convolutions between the different axion spectra and the obtained intrinsic efficiencies of IAXO-D1 and its proposed extension are presented. For that purpose, fitted routines to the different detector efficiencies presented in Appendix A are used.

[18]The K and L emission lines of Argon are: $K_{\alpha_1} = 2957.7$ eV; $K_{\alpha_2} = 2955.63$ eV; $K_{\beta_1} = 3190.5$ eV [34, 37].
[19]Implemented in the GDML files as 3.96 μm of Mylar plus 0.04 μm of Al.

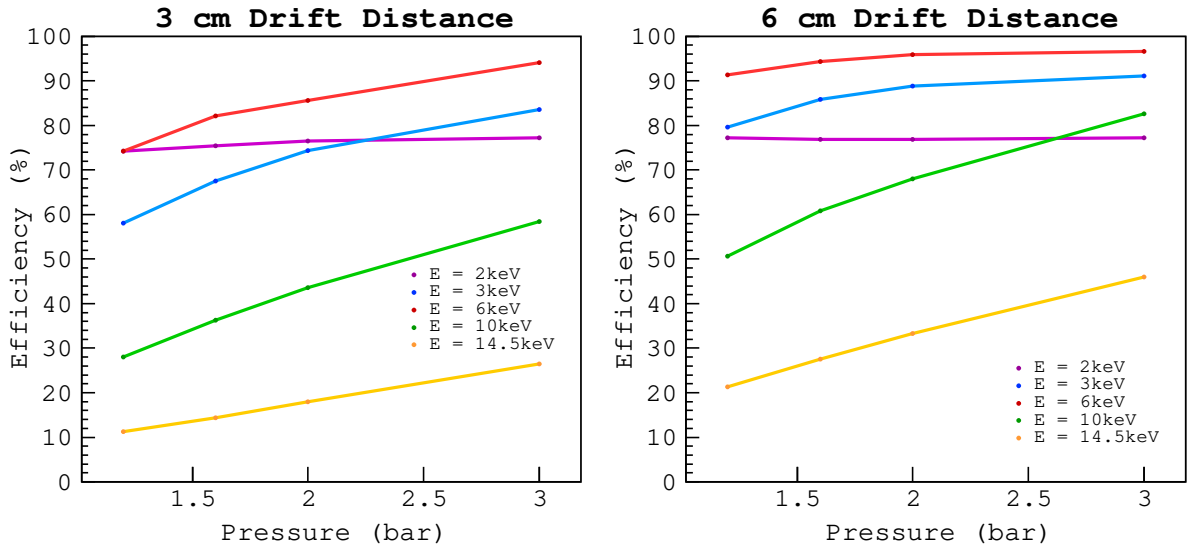

Figure 10: Comparison of intrinsic efficiency values in % with respect to the pressure values used on the simulations for different energy lines between 3cm (left) and 6cm (right) drift chambers.

The ABC flux, that has no analytical expression, but it can be computed from available libraries [20, 39], as already shown in Fig. 3, yields an extensive list of discrete axion flux values across the 0-to-12 keV energy range. Fig. 11 shows the nominal spectrum presented in purple and the folded efficiency results for different detector configurations under study. Since the transmittance of the mylar window is negligible at low energies, the signal coming from ABC axions suffers a considerable loss at low energies ($\lesssim 1$ keV). Nevertheless, at higher energies, the original spectrum is matched by the resulting curves. Overall, regardless of the chosen detector configuration, the efficiency of detection for non-hadronic axions is between $50-57\%$.

Next, the results for the Primakoff flux (which has an analytical expression, as depicted in Eq. 6) are displayed in Fig. 12, where the Primakoff flux has been plotted in purple, and folded efficiencies in other colors. In this case, doubling the size of the chamber's drift distance can increase the probability of detecting axion signals from the hadronic model from the nominal 72% of IAXO-D1 prototype up to 85% for a 6 cm drift chamber at 3 bar of pressure.

Finally, in the case of axion-nucleon flux, a set of arguments have been considered in order to propose a Gaussian expression to analytically define and subsequently convolute the differential flux from the axion-nucleon coupling expected at the Earth. First, $\sigma(T) = E^* \sqrt{\frac{kT}{m_{Fe57}}}$ is the standard deviation parameter of the axion emission spectrum owing to Doppler broadening caused by the thermal motion of ^{57}Fe nuclei in the hot solar interior (FWHM $= 2.35\,\sigma(T) \sim 5$ V thus, $\sigma(T) \sim 2.13$)[14]. $E_\gamma = E^* = 14.4$ keV is the transition energy at which the spectrum is centered, T refers to the temperature at the location in the Sun where the axion is produced, and m_{Fe57} refers to the mass of the ^{57}Fe nucleus. Lastly, the Gaussian defined by the previous parameters has been multiplied by $\Phi_{\rm aN} = 4.56 \cdot 10^{23}\,(g_{\rm aN}^{\rm eff})^2\,{\rm cm}^{-2}{\rm s}^{-1}$, which is the integrated

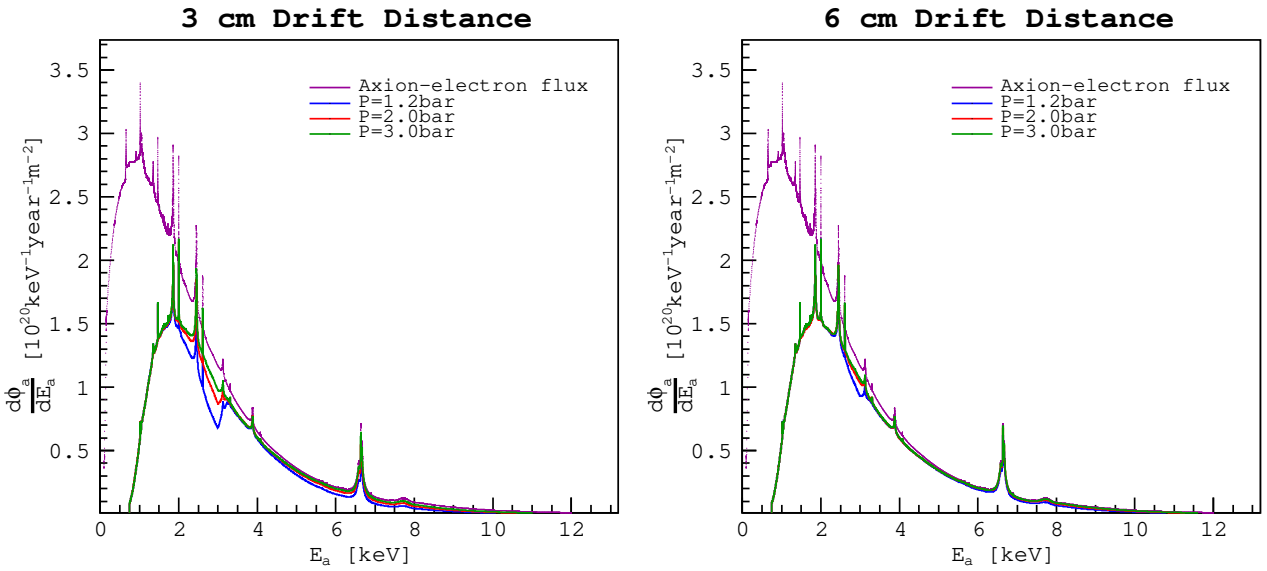

Figure 11: Left: spectra result of the convolution of axion - electron spectrum with normalized efficiency curves at P = 1.2, 2, 3 bar using 3 cm drift distance chamber. Right: spectra result of the convolution of axion - electron spectrum with normalized efficiency curves at P = 1.2, 2, 3 bar using 6 cm drift distance chamber.

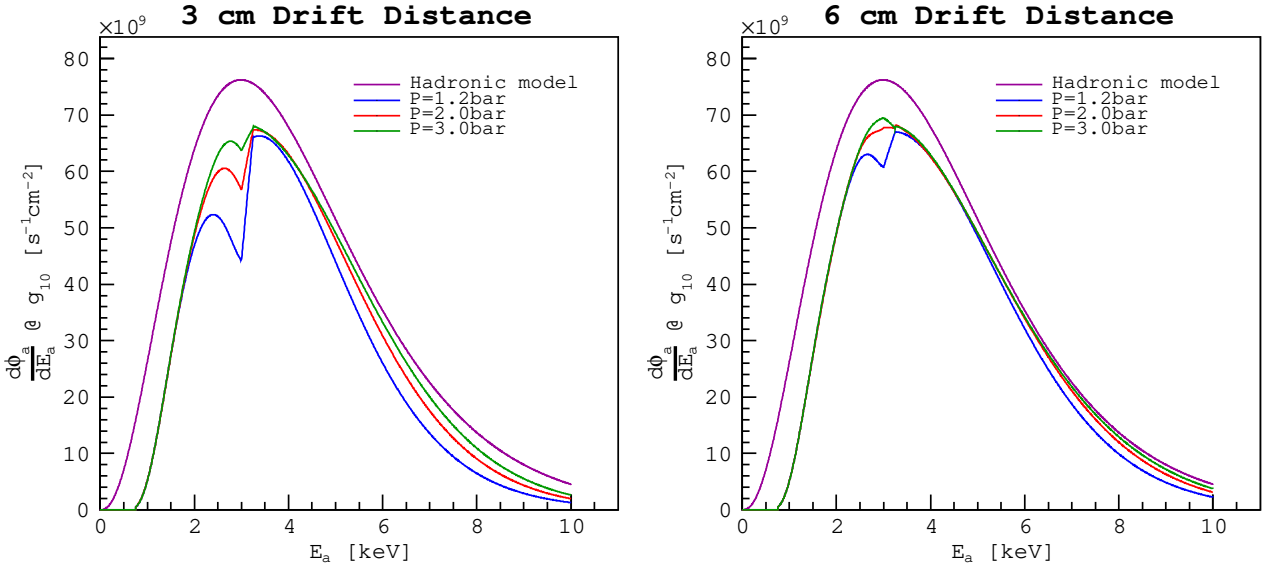

Figure 12: Left: spectra result of the convolution of axion - nucleon spectrum with normalized efficiency curves at P = 1.2, 2, 3 bar using 3 cm drift distance chamber. Right: spectra result of the convolution of axion - nucleon spectrum with normalized efficiency curves at P = 1.2, 2, 3 bar using 6 cm drift distance chamber.

axion-nucleon flux with respect to the energy, where g_{aN}^{eff} is the effective nucleon coupling[20].

[20]Recent calculations lead to an improved bound on the axion effective coupling with nucleons, $g_{aN}^{eff} \leqslant 1.89 \cdot 10^{-6}$, referred to as the solar bound on g_{aN}^{eff} [14, 40].

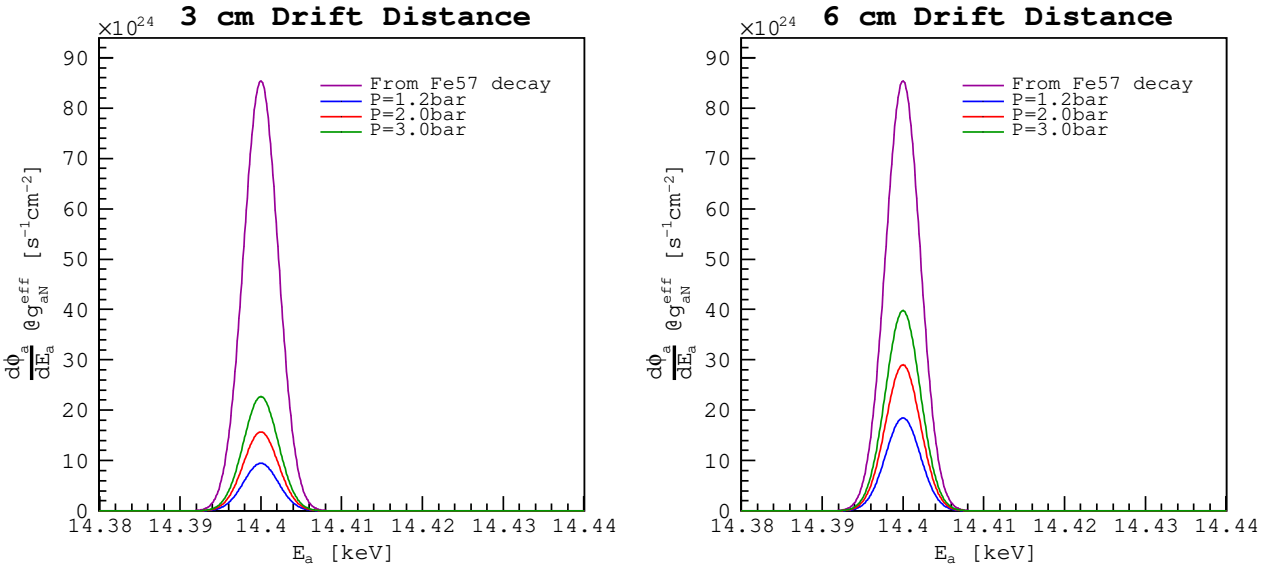

Figure 13: Left: spectra result of the convolution of axion-nucleon spectrum with normalized efficiency curves at P = 1.2, 2, 3 bar using 3 cm drift distance chamber. Right: spectra result of the convolution of axion - nucleon spectrum with normalized efficiency curves at P = 1.2, 2, 3 bar bar using 6 cm drift distance chamber.

All these considerations lead to the following expression:

$$\frac{d\Phi_{aN}(E_a)}{dE_a} = \Phi_{aN} \cdot \frac{1}{\sqrt{2\pi}\sigma(T)} \cdot e^{-\frac{(E_a - E_\gamma)^2}{2\sigma(T)^2}}. \tag{9}$$

However, g_{aN}^{eff} has been suppressed by dividing expression 9 by $(g_{aN}^{eff})^2$ in order to eliminate its dependency on the simulation results. The theoretical spectrum is shown in purple in Fig. 13, along with the curves obtained from the convolution. From Fig. 13, it is clear that a drift distance of 6 cm is more efficient at detecting axion-nucleon signals, even a factor 4 better if we consider the 3 bar pressure setup.

In order to not only provide a visual comparison of the differential spectra corresponding to different detector sizes but also quantify the difference between them, the spectra have been integrated over the entire energy range using the trapezoid rule[21] in a ROOT macro, and relative percentages with respect to each nominal spectrum have been calculated. Table 1 shows the corresponding percentages obtained.

For example, for the axion-nucleon coupling, the use of a Micromegas drift chamber of 6 cm instead of a conventional 3 cm at 3 bar pressure allows for a $\sim$ 20 % increase in detection efficiency. Relative gains for the different pressures and drift chamber lengths can be seen in Appendix B.

[21] A numerical method for approximating the definite integral of a function by dividing the area under the curve into a series of trapezoids and summing their areas [41]. Errors can be estimated using finite difference approximations. However, due to the complexity and time-consuming nature of this method, it has not been undertaken in this study.

P (bar)	ABC flux	Primakoff flux	aN flux	P (bar)	ABC flux	Primakoff flux	aN flux
1.2	49.62 %	71.53 %	11.06 %	1.2	54.56 %	81.10 %	21.61 %
2.0	53.58 %	79.26 %	18.35 %	2.0	56.04 %	84.42 %	33.94 %
3.0	55.46 %	83.04 %	26.56 %	3.0	56.66 %	85.64 %	46.57 %

Table 1: Comparison of integrated fluxes with respect to the nominal value of each flux. Left: for 3 cm drift distance. Right: for 6 cm drift distance.

5. Geant4 Simulations for axion discovery

This chapter performs a full axion spectra simulation for the three axion coupling considered in this work: axion-photon, axion-electron and axion-nucleon; in contrast with the monoenergetic simulations and fitting routines presented in the previous chapter. It is important to note that the axion-photon conversion probability is assumed to be equal to 1 (see Appendix C for an introduction to axion conversion probability). This chapter is divided into two subsections. In the first subsection, the energy depositions from the three raw spectra are simulated, and in the second subsection, these simulations are analyzed with REST to apply the contour experimental parameters and simulate the diffusion and attachment inherent of Micromegas detectors.

5.1. Nominal photon flux at the detector

With the objective of simulating the nominal photon fluxes, the GDML files describing the geometry and the RML files containing the simulation conditions described in Section 4.2 have been reused. However, instead of launching simulations using a monoenergetic photon flux, a TH1D histogram has been used to define each spectrum and provide RestG4 with a probability distribution of the arriving photons. The resulting photons in the detector have been renormalized so that it is adequately scaled in accordance with the originating spectrum. Simulations for P=1.2 and 2.0 bar have been performed for the IAXO-D1 prototype and the proposed extension, and the statistical errors have been calculated, by defining the error bar for each energy bin as the square root of the bin count[22]. The number of events to be registered in the detector is set to $500,000$ in the case of ABC and Primakoff fluxes. Nevertheless, in the case of axion-nucleon flux this number is equal to $200,000$ since the nature of its spectrum is quasi-monoenergetic.

The results for the ABC photon flux are presented in Fig. 14. It is evident that the spectra obtained in Fig. 14 agree with the convoluted spectra depicted in Fig. 11 of Section 4.2.1.

The plots resulting from the Primakoff photon flux are presented in Fig. 15. Here, as in Fig. 12 of Section 4.2.1 the results are consistent with each other and a clear improvement of efficiency can be obtained by doubling the nominal drift distance of the IAXO-D1 prototype

[22]This method is based on the properties of the Poisson distribution. For a histogram where the counts in each bin are large enough to assume a normal distribution approximation, the standard deviation of the counts in each bin can be estimated using the square root of the counts [42, 43].

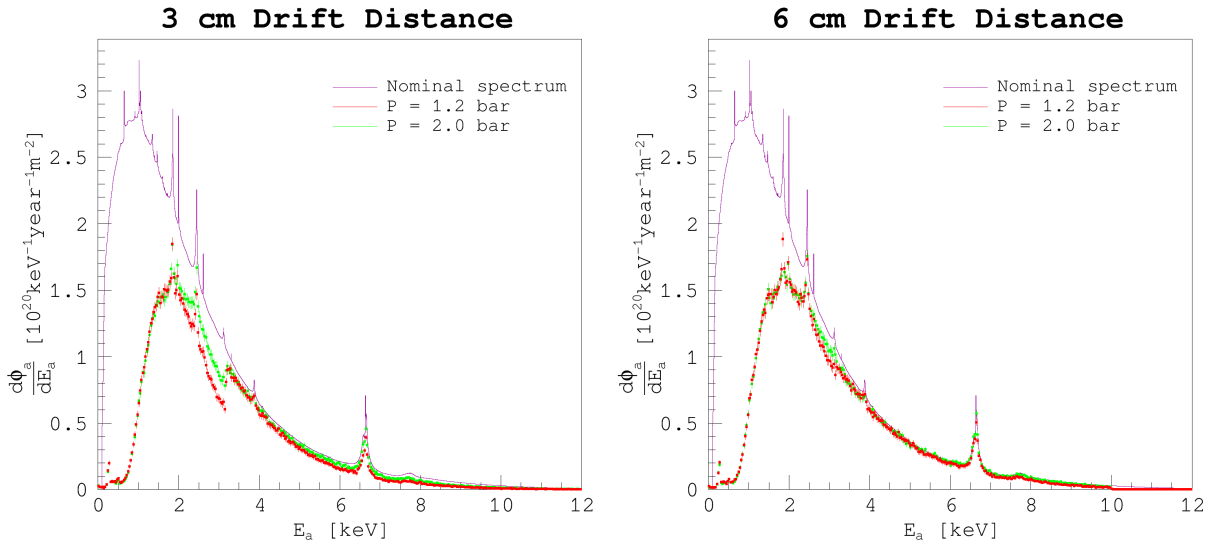

Figure 14: Left: histogram of the nominal ABC differential flux together with its simulations at 1.2 and 2.0 bars using the 3 cm drift chamber. Right: histogram of the nominal ABC differential flux together with its simulations at 1.2 and 2.0 bars using the 6 cm drift chamber.

and increase the operating pressure of the detector. Specially around the Argon escape peak and at energies above 5 keV.

Finally, the simulations corresponding to the axion-nucleon photon flux peaking around 14.4 keV are presented in Fig. 16. Once more, the obtained results are in total agreement with curves presented in Fig. 13 of Section 4.2.1. The secondary excitations produced by this peak

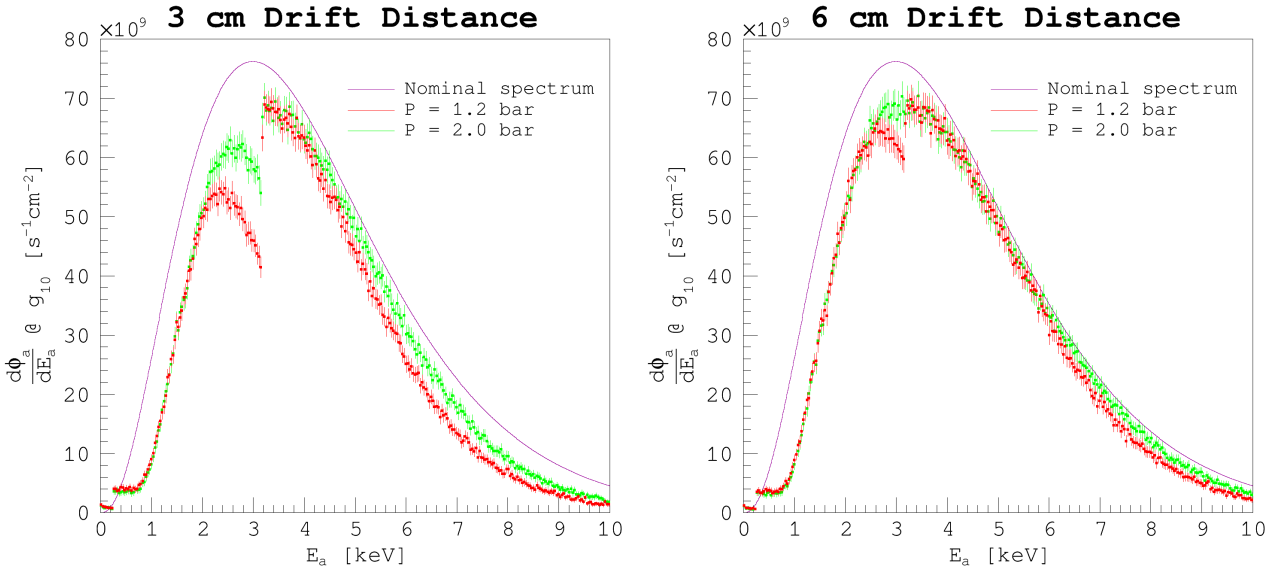

Figure 15: Left: histogram of the nominal Primakoff differential flux together with its simulations at 1.2 and 2.0 bar using the 3 cm drift chamber. Right: histogram of the nominal Primakoff differential flux together with its simulations at 1.2 and 2.0 bar using the 6 cm drift chamber.

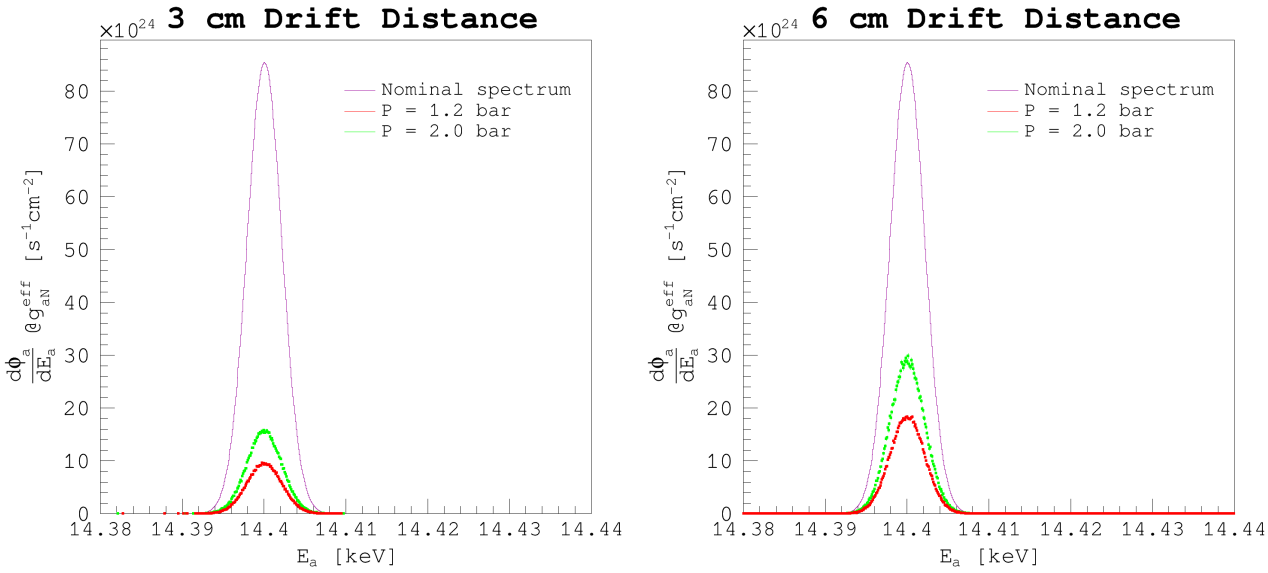

Figure 16: Left: histogram of the nominal axion-nucleon differential flux together with its simulations at 1.2 and 2.0 bar using the 3 cm drift chamber. Right: histogram of the nominal axion-nucleon differential flux together with its simulations at 1.2 and 2.0 bar using the6 cm drift chamber.

have not been yet added in Fig. 16, but for clarity, they will be presented and fitted in the following subsection.

5.2. Study of the detector response

In order to complete the study conducted in this work, the spectra obtained in the previous subsection have been analyzed using REST software[23] to include the effect of the detector's energy resolution and the diffusion process. This has been performed for operational pressure of 1.2 bar, as it is an experimental setup already used in the data takings at the IAXO-Lab (see [44]) and for 2.0 bar since it corresponds to the maximum pressure difference that the present cathode window design can withstand.

The first step of the analysis involves extracting information about energy deposits generated by primary events from the Geant4 Monte Carlo simulations performed using RestG4, which have already been presented in the previous section. This way, hits which include the physical process and geometry volume where the interaction took place are stored. The electromagnetic interactions and physics processes taken into account in the analysis performed in this section have been introduced in Sections 4.1.1 and 4.1.2 and aim to reproduce with fidelity the detector energy resolution measured in the laboratory by means of energy calibrations of the IAXO-D1 prototype. In particular, this analysis introduces a stochastic smearing[24] on the energy of the

[23] All the analysis processes used can be found in REST processes.

[24] A statistical fluctuation or blurring effect that occurs in measurements due to inherent randomness or uncertainty in the processes involved [45].

hits for each registered even. This way, the total energy of each event has been re-distributed following a Gaussian shaped function. The smearing process uses as an input experimental calibrations [32, 44] of the IAXO-D1 prototype (see Fig. 7). In particular, calibrations with the ^{55}Fe [37], from which the experimental energy resolution of the detector is extracted, typically $\sim 20\%$ [44]. For simplicity, despite the possibility that the energy resolution of the detector could slightly differ for a 6 cm drift distance, it has been considered as a good approximation to keep the same energy resolution for both chamber sizes[25]. Moreover, this parameter could be easily adjusted in the results obtained once the new prototype with 6 cm drift is properly calibrated experimentally.

A third analysis process has been added in order to emulate the electron diffusion in the gaseous medium. It uses *Magboltz* [47] to compute transport properties of electrons in the gas mixture through *Garfield++* toolkit [48] which is integrated in REST. This process uses the longitudinal and transverse coefficients of the gas mixture used in the simulations to emulate the relative deviation of electrons from their original positions, supposedly caused by primary ionization [49]. Therefore, the energy of each hit is converted to the corresponding number of primary electrons that would be produced in the ionization process. At this point, each electron corresponds to a new hit, and the process randomly deviates the coordinates of the electrons following a Gaussian distribution related to the gas parameters, longitudinal and transverse diffusion coefficients, and the distance to the readout plane. This process also includes the effect of electron attachment explained in Section 4.1.1, and the number of primary electrons produced is related to the energy deposited, according to the work-function (the W-value). The parameters that must be introduced manually for this process are the gas mixture and pressure, and the electric field, 145 V/cm of the drift region[26]. With these parameters, REST can internally calculate the gas properties and the drift velocity. In these studies, the same electric field value has been set for the 3 cm and the 6 cm drift chambers. However, in the case of 6 cm, that particular setting will need from experimental data validation. It is likely that the electric field will need to increase in order to reduce the diffusion effect due to the larger distance that electrons travel.

Applying the whole analysis chain described above, several calibration simulations with ^{55}Fe have been performed. The purpose of this has been to compare the current experimental spectrum (already depicted in Fig. 7) with the resulting calibration curves from the simulations. This analysis has been done re-normalizing the simulations such that the maxima of the peaks at 5.9 keV match. Fig. 17 shows different energy resolutions in the smearing process, specifically 20 % (green) and 30 % (orange) in comparison to an experimental calibration (blue) of the IAXO-D1 prototype with an ^{55}Fe source. Then, the simulation plots have been re-scaled to match the height of the experimental iron peak so as to show the impact on the FWHM, and

[25] Estimation based on comparison with larger TPC chamber such as the TREX-DM Micromegas-based TPC (see [46]).

[26] Value calculated for the 3 cm drift distance TPC considering a cathode voltage of 750 V and a mesh voltage equal to 315 V, conservative values for data takings as the ones perform for [44].

as seen in Fig. 17, they are in complete agreement.

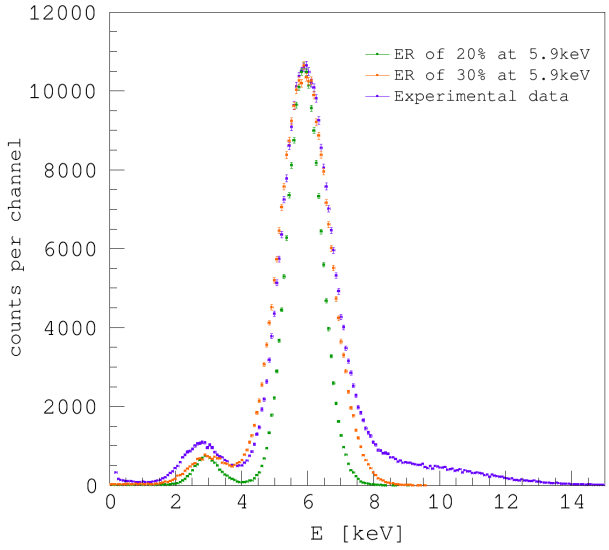

Figure 17: ^{55}Fe simulations applying different energy resolutions (ER) at 5.9 keV, iron's main emission line [37]: ER=20 % (green) corresponds to the nominal value used in this work, and ER=30 % (orange) to the resolution calculated from the experimental data (purple) in Fig. 7 ($\sim$ 30 %). The same experimental spectrum shown in Fig. 7 is depicted again.

From Fig. 17 is clear that the process of smearing and electron transport in the gas of IAXO-D1 has to be tuned for each individual detector. In the following Section, a nominal 20% energy resolution has been chosen, which is a value reachable in normal operation conditions with the IAXO-D1 prototype. The current 30 % energy resolution showed by this particular IAXO-D1 prototype is under investigation and could be related to a production quality issue of that particular readout plane.

5.3. Results from analysis of the simulation

In this section, the resulting analyzed spectra are presented. Histograms shown in Chapter 5.2 are used as input. Photon fluxes from the axion-electron coupling are presented in Fig. 18, and are in accordance with the corresponding simulated spectra in Fig. 14. Nevertheless, it is noteworthy that the blurring produced by the smearing and diffusion processes makes the characteristic peaks of the ABC flux to completely disappear, which was anticipated due to the energy resolution of the IAXO-D1 prototype. However, the peak around 6 keV is slightly noticeable, especially for the 6 cm drift distance chamber, and the Argon escape peak is totally blurred except for the case of 6 keV peak, where it can still be inferred.

Primakoff spectra are shown in Fig. 19, also in accordance with the corresponding simulated spectra in Fig. 15, being the hit events redistributed according to the detector's features. Here, just for the setup corresponding to the 3 cm chamber at 1.2 bar the Argon escape peak can be seen. In addition, the behaviour at high energies is more efficient at 2.0 bar than at 1.2 bar, as expected, and the nominal spectrum remains within the uncertainty errors of the 2.0 bar curve.

The axion-nucleon spectra resulting from this analysis are displayed in Fig. 20. The nominal axion-nucleon spectrum has been omitted for clarity, as the flux in the analyzed data is signifi-

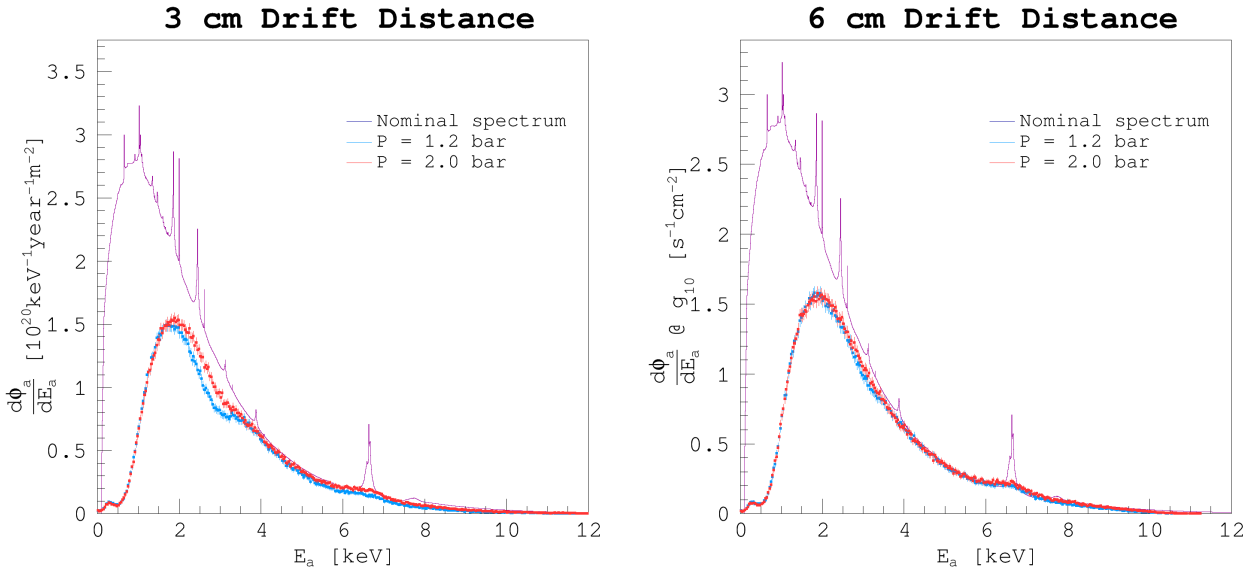

Figure 18: Left: histogram of the nominal ABC differential flux together with the analyzed spectra at 1.2 and 2.0 bar using the 3 cm drift chamber. Left: histogram of the nominal ABC differential flux together with the analyzed spectra at 1.2 and 2.0 bar using the 6 cm drift chamber.

cantly lower than the detected with the IAXO-D1 prototype, as result of detector efficiency and energy resolution. The detector distributes the counts in a much wider Gaussian than the M1 ^{57}Fe transition line arriving from the Sun. Fig. 20 also shows secondary excitations produced in the detector.

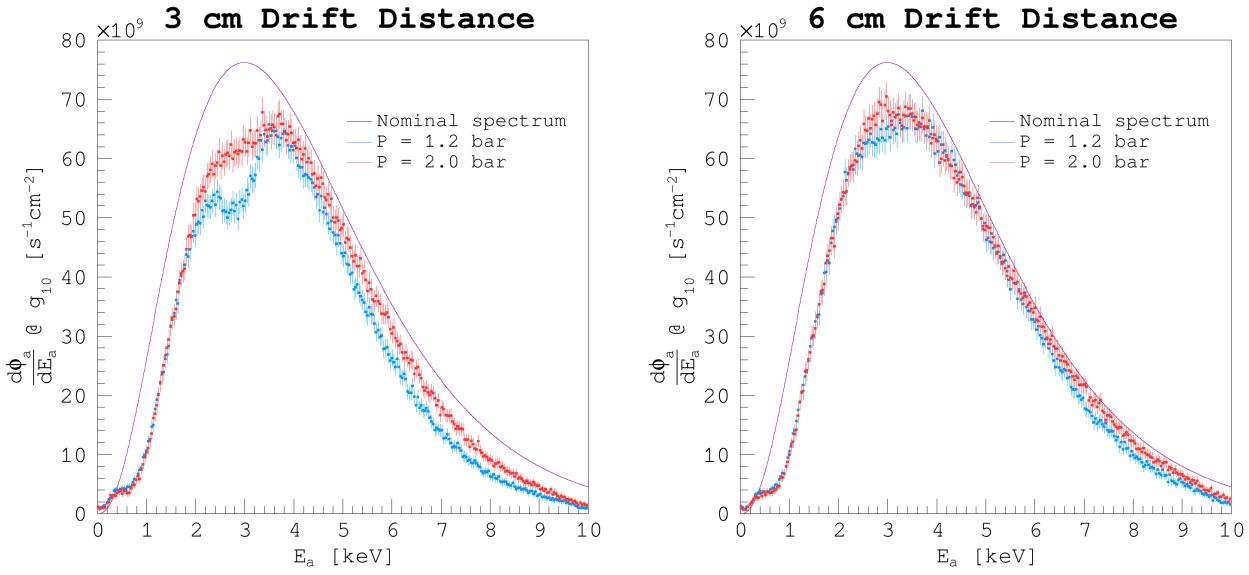

Figure 19: Left: histogram of the nominal Primakoff differential flux together with the analyzed spectra at 1.2 and 2.0 bar using the 3 cm drift chamber. Left: histogram of the nominal Primakoff differential flux together with the analyzed spectra at 1.2 and 2.0 bar using the 6 cm drift chamber.

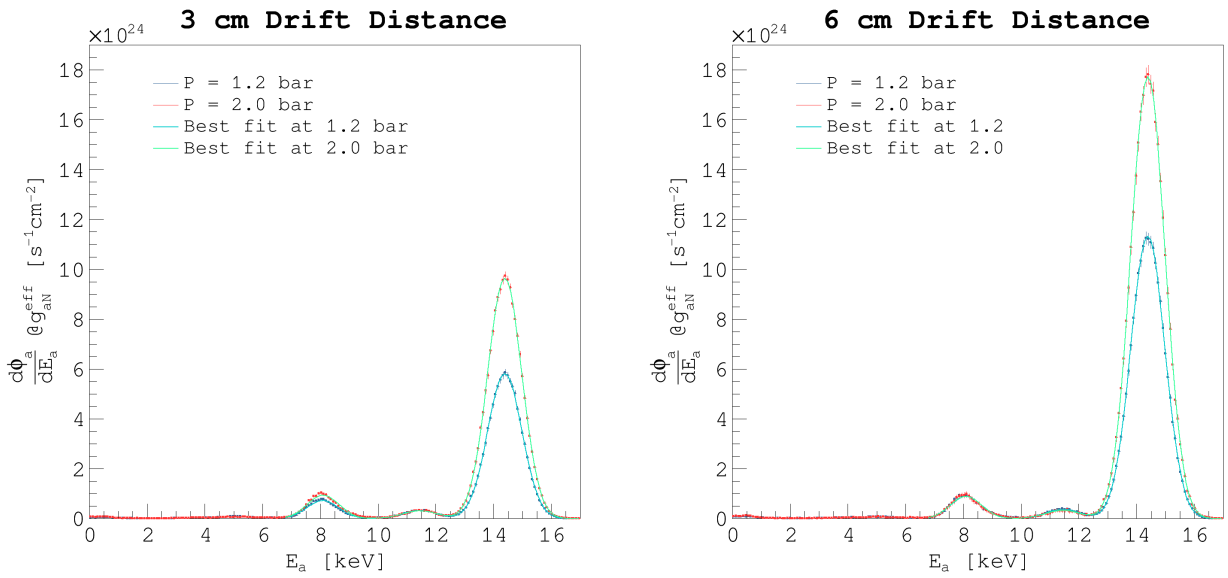

Figure 20: Left: histogram of the axion-nucleon flux together with the analyzed spectra at 1.2 and 2.0 bar using the 3 cm drift chamber. Left: histogram of the axion-nucleon together with the analyzed spectra at 1.2 and 2.0 bar using the 6 cm drift chamber. Each of the four spectra has been fitted with a sum of three Gaussian functions.

3 cm drift distance chamber

P(bar)		**Cu K_{α_1}**	**Escape peak**	**M1 ^{57}Fe line**
1.2	Mean (keV)	$(8090 \pm 9) \times 10^{-3}$	$(11450 \pm 2) \times 10^{-2}$	$(14390 \pm 3) \times 10^{-3}$
	ER (%)	$(158 \pm 3) \times 10^{-1}$	$(122 \pm 3) \times 10^{-1}$	$(971 \pm 4) \times 10^{-2}$
2.0	Mean (keV)	$(8100 \pm 9) \times 10^{-3}$	$(1146 \pm 2) \times 10^{-2}$	$(14390 \pm 3) \times 10^{-3}$
	ER (%)	$(159 \pm 2) \times 10^{-1}$	$(125 \pm 4) \times 10^{-1}$	$(966 \pm 3) \times 10^{-2}$

6 cm drift distance chamber

P(bar)		**Cu K_{α_1}**	**Escape peak**	**M1 ^{57}Fe line**
1.2	Mean (keV)	$(810 \pm 1) \times 10^{-2}$	$(1146 \pm 2) \times 10^{-2}$	$(14400 \pm 3) \times 10^{-3}$
	ER (%)	$(157 \pm 3) \times 10^{-1}$	$(121 \pm 4) \times 10^{-1}$	$(968 \pm 4) \times 10^{-2}$
2.0	Mean (keV)	$(809 \pm 2) \times 10^{-2}$	$(1145 \pm 3) \times 10^{-2}$	$(14400 \pm 3) \times 10^{-3}$
	ER (%)	$(156 \pm 4) \times 10^{-1}$	$(126 \pm 7) \times 10^{-1}$	$(968 \pm 4) \times 10^{-2}$

Table 2: Fits for the axion-nucleon spectra.

Remembering that Argon's main emission line is ~ 2.95 keV, a fast calculation can be done to proof that the peak around ~ 11.5 keV is the escape peak produced by the ^{57}Fe emission line. In addition, the peak at ~ 8 keV corresponds to the Copper fluorescence[27]. The results of the fits performed in Fig. 20 are presented in table 2.

In Table 2, the mean energy values and their corresponding errors from the fits are shown. Also, the energy resolutions are given with their corresponding errors (see [43]). These fits

[27] K emission lines of Cu are $K_{\alpha_1} = 8047.78\,eV$ and $K_{\alpha_2} = 8027.83\,eV$ [37].

clearly show that the higher the energy, the better the resolution is. Furthermore, the fits have been performed for the different pressure settings and both chamber sizes.

6. Conclusions and future steps

In this work, the intrinsic efficiency of the IAXO-D1 prototype and its impact on detecting different axion spectra have been studied, allowing for the evaluation of the detection potential of both, the present detector and a proposed enhancement with double drift distance. Consequently, a better understanding of the physics within the TPC has been achieved through a series of calculations and simulations. These included studying energy deposition in the active gas, the effect of smearing due to detector resolution, simulation of electron diffusion, and hits detection in the readout plane. These steps form the indispensable beginning of an analysis process chain, and it results very appealing to extend this research further, both computationally and experimentally.

The scope of this work was to increase the axion-nucleon sensitivity of the IAXO experiment, which has been proven by means of increasing the operating pressure of the current IAXO-D1 prototype or by enhancing the current design with a 6 cm lenght drift chamber TPC Micromegas . These simulations showcase a factor 3-to-4 enhancement depending on the gas pressure to operate the detector. In addition, the design of a new cathode window capable of withstanding a pressure difference greater than $\Delta P = 2$ bar could significantly enhance the detection efficiency by allowing for higher gas pressures. This dual approach, would increase the intrinsic detection efficiency as it is shown in Figs. 18, 19 and 20. It is remarkable that this route of action enhances not only the axion-nucleon coupling case, but also the axion-electron and axion-photon couplings. The development and testing of such enhanced detector and cathode window should be focus of future experimental work.

It would also be recommended to emulate the entire electronic chain in the analysis, including the acquisition system of IAXO-D1 , along with track and signal reconstruction. This would allow for the introduction of more parameters that affect efficiency of detection, such as electronic noise, for a more realistic reconstruction of events.

For a better understanding of the the sensitivity impact of IAXO-D1 pressure setting and the proposed 6 cm length drift enhancement, it would be advisable to proceed with a background simulation, incorporating shielding into the geometry files. Identifying the sources and characteristics of background signals also facilitates the design and optimization of the detector to minimize background interference.

Lowering the threshold remains a priority in order to detect axion signals, especially in the case of non-hadronic axions. The use of Gas Electron Multipliers (GEMs) [50] between the cathode window and the mesh is a nice option. However, as shown in Fig. 9, the restrictive factor to lower the detertor threshold is the use of a Mylar window. Other gas mixtures, such as Argon-5% isobutane or Xenon-Neon-Isobutane should also be explored, since higher

percentage of quencher can improve significantly the energy resolution of the detectors and Xenon mixtures might be able to further increase the detector efficiency at energies above 4 keV. Such data would allow to fine-tune the setup, providing a clearer understanding of how to achieve the desired axion sensitivity, both for the present IAXO-D1 prototype and its proposed enhancement.

As a final step it would be recommended to procure with a full IAXO simulation, including the conversion probability, optics efficiency and solar disk emission of axions for each axion coupling.

In summary, this research has laid a solid foundation for future detector developments in IAXO-D1. The proposed enhancements and next steps are crucial for improving the performance and accuracy of the detection system.

References

[1] D.F.J. Kimball and K. van Bibber, editors. *The Search for Ultralight Bosonic Dark Matter*. Springer Nature, 2023.

[2] Y. Akrami et al. Planck2018 results: Vii. isotropy and statistics of the cmb. *Astronomy & Astrophysics*, 641, 2020.

[3] Nathalie Deruelle and Jean-Philippe Uzan. 605The Lambda-CDM model of the hot Big Bang. In *Relativity in Modern Physics*. Oxford University Press, 08 2018.

[4] A.B. Aleksandrov et al. Search for weakly interacting massive dark matter particles: state of the art and prospects. *Physics-Uspekhi*, 64(9):861, Sept. 2021.

[5] L. Covi et al. Gravitino dark matter and general neutralino nlsp. *Journal of High Energy Physics*, 2009(11):003, Nov. 2009.

[6] S. Jarman. Primordial black holes limited to 40% of dark matter. *Physics World*, 31(11):4, Nov. 2018.

[7] P. Sikivie. Dark matter axions. *Int. Journal of Modern Physics A*, 25(02n03), 2010.

[8] R. D. Peccei and Helen R. Quinn. CP conservation in the presence of pseudoparticles. *Phys. Rev. Lett.*, 38:1440–1443, Jun 1977.

[9] R. D. Peccei and Helen R. Quinn. Constraints imposed by CP conservation in the presence of pseudoparticles. *Phys. Rev. D*, 16:1791–1797, Sep 1977.

[10] I. G. Irastorza et al. Future axion searches with the international axion observatory (iaxo). *Journal of Physics: Conference Series*, 460(1):012002, oct 2013.

[11] G. Pignol et al. Measurement of the permanent electric dipole moment of the neutron. *Phys. Rev. Lett.*, 124:081803, Feb. 2020.

[12] G. Pignol and P. Schmidt-Wellenburg. The search for the neutron electric dipole moment at psi, 2021.

[13] F. Chadha-Day, J. Ellis, and D. J. E. Marsh. Axion dark matter: What is it and why now?, 2022.

[14] CAST collaboration. Search for 14.4 kev solar axions emitted in the m1-transition of 57fe nuclei with cast. *Journal of Cosmology and Astroparticle Physics*, 2009(12):002, dec 2009.

[15] CAST Collaboration. An improved limit on the axion–photon coupling from the cast experiment. *Journal of Cosmology and Astroparticle Physics*, 2007(04):010, apr 2007.

[16] L. Di Luzio et al. The landscape of qcd axion models. *Physics Reports*, 870, 2020.

[17] H. Leutwyler. The ratios of the light quark masses. *Physics Letters B*, 378(1–4):313–318, June 1996.

[18] P. Sikivie. Experimental Tests of the Invisible Axion. *Phys. Rev. Lett.*, 51:1415–1417, 1983.

[19] K. Zioutas et al. Axion searches with helioscopes and astrophysical signatures for axion(-like) particles. *New Journal of Physics*, 11(10):105020, oct 2009.

[20] J. Redondo. Solar axion flux from the axion-electron coupling. *Journal of Cosmology and Astroparticle Physics*, 2013(12):008–008, December 2013.

[21] F Combes. Properties of dark matter haloes. *New Astronomy Reviews*, 46(12):755–766, 2002.

[22] Physics: Not a wisp of evidence. *Nature*, 465(7296):271–271, May 2010.

[23] I.G. Irastorza and J. Redondo. New experimental approaches in the search for axion-like particles. *Progress in Particle and Nuclear Physics*, 102:89–159, September 2018.

[24] García-Barceló et al. Methods and restrictions to increase the volume of resonant rectangular-section haloscopes for detecting dark matter axions. *Journal of High Energy Physics*, 2023(8), August 2023.

[25] The ADMX Collaboration. Axion dark matter experiment: Detailed design and operations. *Review of Scientific Instruments*, 92(12), December 2021.

[26] Benjamin M. Brubaker. First results from the haystac axion search, 2018.

[27] CAST Collaboration. New cast limit on the axion–photon interaction. *Nature Physics*, 13(6):584–590, Jun 2017.

[28] A. Abeln et al. Conceptual design of babyiaxo, the intermediate stage towards the international axion observatory. *Journal of High Energy Physics*, 2021, 05 2021.

[29] H. J. Hilke. Time projection chambers. *Rept. Prog. Phys.*, 73:116201, 2010.

[30] Y. Giomataris, Ph. Rebourgeard, J.P. Robert, and G. Charpak. Micromegas: a high-granularity position-sensitive gaseous detector for high particle-flux environments. *Nuclear Instruments and Methods in Physics Research Section A: Accelerators, Spectrometers, Detectors and Associated Equipment*, 376(1):29–35, 1996.

[31] S. Andriamonje et al. Development and performance of microbulk micromegas detectors. *Journal of Instrumentation*, 5(02):P02001, feb 2010.

[32] E. Ruiz-Chóliz. *Ultra-low background Micromegas X-ray detectors for Axion searches in IAXO and BabyIAXO*. PhD thesis, Zaragoza U., 2019.

[33] B. Beltrán. *A TPC (time projection chamber) for axion searches in the CAST experiment at CERN*. PhD thesis, Zaragoza U., 2006.

[34] Glenn F Knoll. *Radiation detection and measurement*. John Wiley & Sons, 2010.

[35] Javier Galan on behalf of the IAXO collaboration. Exploring the sun's core with babyiaxo. In *Proceedings of TAUP2021*, Valencia, Spain, 2021.

[36] I. Antolín. Repository with master's thesis code. `https://github.com/IAntolin/Study-and-characterization-of-MM-for-their-use-in-IAXO-.git`.

[37] A.C. Thompson. *X-ray Data Booklet*. Lawrence Berkeley National Laboratory, University of California, 2001.

[38] Gullikson E. M. Henke, B. L. and J. C. Davis. X-ray interactions with matter. `https://henke.lbl.gov/optical_constants/`.

[39] CAST collaboration. Cast constraints on the axion-electron coupling. *Journal of Cosmology and Astroparticle Physics*, 2013(05), 2013.

[40] Di Luzio et al. Probing the axion–nucleon coupling with the next generation of axion helioscopes. *The European Physical Journal C*, 2022.

[41] P. J. Davis and P. Rabinowitz. Chapter 2 - approximate integration over a finite interval. In *Methods of Numerical Integration*, pages 51–198. Academic Press, 1984.

[42] Luca Lista. *Statistical Methods For Data Analysis*. Springer, 2017.

[43] Gerhard Bohm and Günter Zech. *Introduction to statistics and data analysis for physicists*, volume 1. Desy Hamburg, 2010.

[44] K. et al. Altenmüller. Background discrimination with a Micromegas detector prototype and veto system for BabyIAXO. *Front. in Phys.*, 12:1384415, 2024.

[45] AL MacKinnon and IJD Craig. Stochastic simulation of fast particle diffusive transport. *Astronomy and Astrophysics (ISSN 0004-6361), vol. 251, no. 2, Nov. 1991, p. 693-699. Research supported by SERC.*, 251:693–699, 1991.

[46] F. J. Iguaz et al. Trex-dm: a low background micromegas-based tpc for low-mass wimp detection. *Journal of Physics: Conference Series*, 718:042026, May 2016.

[47] S. F. Biagi. Magboltz simulation program. `https://magboltz.web.cern.ch/magboltz/`.

[48] H. Schindler and R. Veenhof. Garfield++ program. `https://gitlab.cern.ch/garfield/garfieldpp`.

[49] J. Galan et al. Topological background discrimination in the pandax-iii neutrinoless double beta decay experiment. *Journal of Physics G: Nuclear and Particle Physics*, 47(4):045108, March 2020.

[50] Fabio Sauli. The gas electron multiplier (gem): Operating principles and applications. *Nuclear Instruments and Methods in Physics Research Section A: Accelerators, Spectrometers, Detectors and Associated Equipment*, 805:2–24, 2016.

[51] K. van Bibberet al. Design for a practical laboratory detector for solar axions. *Phys. Rev. D*, Apr 1989.

Appendices

A. Fits performed for the intrinsic efficiency.

First, the different efficiencies have been renormalized to range from 0 to 1. Figure 21 shows the polynomial fits performed for the intrinsic efficiency curves.

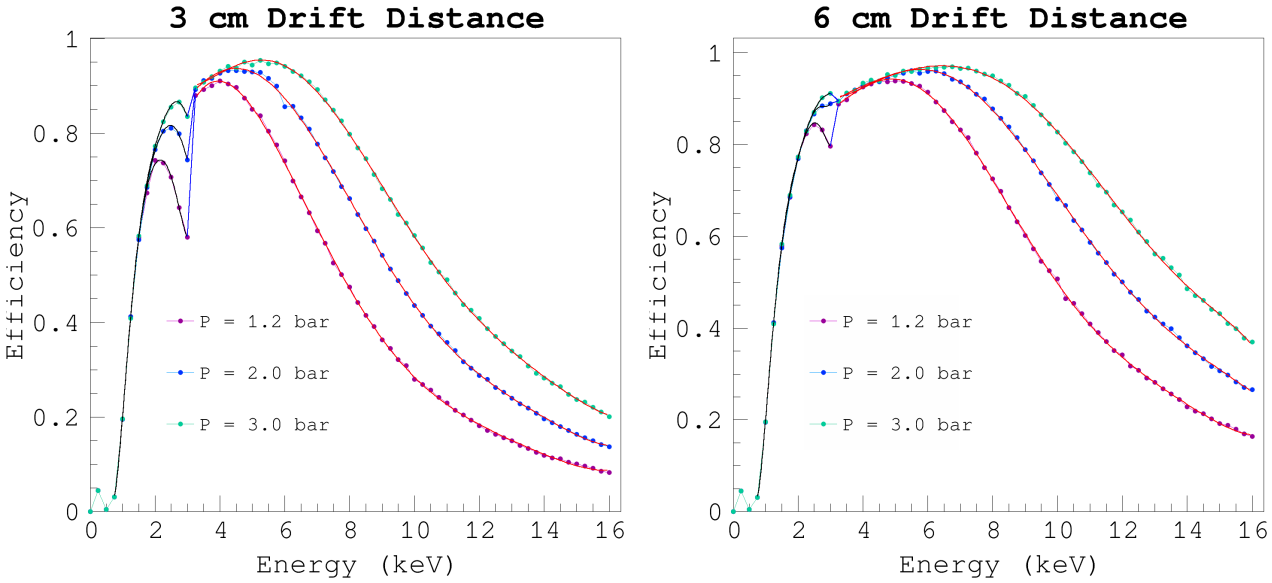

Figure 21: Polynomial fits for the intrinsic efficiency curves at different pressures.

Then, the curves have been fitted within the $[0.75, 16.0]$ keV interval, since the current energy threshold of the detector prototype is approximately 1 keV, mainly limited by the thickness of the cathode window [44], and covers all the energy spectra. This fitting has allowed to define an analytic ROOT function for each efficiency curve that can be evaluated at any energy value. The fitting has been performed in three sections: from 0.75 keV to 3 keV with a 6th-degree polynomial curve, from 3 keV to 3.25 keV with a linear fit to account for the drop due to the Argon escape peak, and from 3.25 keV to 16 keV again with a 6th-degree polynomial curve. This has resulted in a good fit, with the highest chi-square value being 0.000858759 for the third section of the 3.0 bar curve for the 6 cm curve, so the discrepancy between the original efficiency curves and the fitted ones has been considered negligible. Below, the results of the convolutions are presented.

In what follows, all the fit parameters are shown, p_i, according to the polynomial degree (number of parameters = polynomial degree + 1), together with the chi-square (χ^2) functions and the number of degrees of freedom (NDf).

1. Fits corresponding to the 3 cm drift distance chamber:
   For the P = 1.2 bar:

Minimizer is Linear / Migrad
$\chi^2 = 0.000192198$
NDf = 3
$p_0 = 3.23597 \pm 1.40046$
$p_1 = -13.4982 \pm 5.5509$
$p_2 = 20.9072 \pm 8.70498$
$p_3 = -15.3606 \pm 6.94419$
$p_4 = 6.05024 \pm 2.98545$
$p_5 = -1.24157 \pm 0.65867$
$p_6 = 0.104308 \pm 0.0584903$

****
Minimizer is Linear / Migrad
$\chi^2 = 1.47385$e-27
NDf = 0
$p_0 = -3.00733 \pm 17.6918$
$p_1 = 1.19583 \pm 5.65685$

****
Minimizer is Linear / Migrad
$\chi^2 = 0.000669101$
NDf = 46
$p_0 = -1.0901 \pm 0.0586869$
$p_1 = 1.33917 \pm 0.0383021$
$p_2 = -0.313177 \pm 0.00932999$
$p_3 = 0.0312464 \pm 0.00106866$
$p_4 = -0.00145468 \pm 5.80145e-05$
$p_5 = 2.60096e-05 \pm 1.20275e-06$

For the P = 2.0 bar:

Minimizer is Linear / Migrad
$\chi^2 = 0.000109651$
NDf = 3
$p_0 = 2.8759 \pm 1.0578$
$p_1 = -12.0579 \pm 4.19272$
$p_2 = 18.6183 \pm 6.57506$
$p_3 = -13.4771 \pm 5.2451$

$p_4 = 5.18359 \pm 2.25497$
$p_5 = -1.02707 \pm 0.497507$
$p_6 = 0.0823947 \pm 0.044179$

****
Minimizer is Linear / Migrad
$\chi^2 = 5.58674\text{e-}28$
NDf = 0
$p_0 = -1.04569 \pm 17.6918$
$p_1 = 0.596378 \pm 5.65685$

****
Minimizer is Linear / Migrad
$\chi^2 = 0.000766104$
NDf = 45
$p_0 = 0.825095 \pm 0.163623$
$p_1 = -0.221457 \pm 0.129864$
$p_2 = 0.162419 \pm 0.0404954$
$p_3 = -0.0373657 \pm 0.00638106$
$p_4 = 0.00367916 \pm 0.00053877$
$p_5 = -0.000167559 \pm 2.32325e-05$
$p_6 = 2.91525e-06 \pm 4.01663e-07$

For the P = 3.0 bar:

Minimizer is Linear / Migrad
$\chi^2 = 5.27444\text{e-}05$
NDf = 3
$p_0 = 3.21413 \pm 0.733642$
$p_1 = -13.2947 \pm 2.90788$
$p_2 = 20.3491 \pm 4.56017$
$p_3 = -14.658 \pm 3.63777$
$p_4 = 5.59285 \pm 1.56395$
$p_5 = -1.09321 \pm 0.345049$
$p_6 = 0.086087 \pm 0.0306406$

****
Minimizer is Linear / Migrad

χ^2 = 2.4467e-29
NDf = 0
$p_0 = 0.101542 \pm 17.6918$
$p_1 = 0.244536 \pm 5.65685$

****
Minimizer is Linear / Migrad
χ^2 = 0.00069227
NDf = 45
$p_0 = 1.90691 \pm 0.155539$
$p_1 = -1.01403 \pm 0.123448$
$p_2 = 0.372879 \pm 0.0384946$
$p_3 = -0.0629449 \pm 0.00606578$
$p_4 = 0.00524366 \pm 0.00051215$
$p_5 = -0.000214008 \pm 2.20846e-05$
$p_6 = 3.43573e-06 \pm 3.81817e-07$
Value of the fit function at x = 3.25029 is 0.891388

2. Fits corresponding to the 6 cm drift distance chamber:
For the P = 1.2 bar:
Minimizer is Linear / Migrad
χ^2 = 7.33209e-05
NDf = 3
$p_0 = 3.84366 \pm 0.864987$
$p_1 = -16.0833 \pm 3.42849$
$p_2 = 25.234 \pm 5.37659$
$p_3 = -18.9865 \pm 4.28905$
$p_4 = 7.64155 \pm 1.84395$
$p_5 = -1.58559 \pm 0.406824$
$p_6 = 0.133149 \pm 0.0361262$

****
Minimizer is Linear / Migrad
χ^2 = 3.19735e-29
NDf = 0
$p_0 = -0.299875 \pm 17.6918$
$p_1 = 0.365322 \pm 5.65685$

****

Minimizer is Linear / Migrad

$\chi^2 = 0.000698911$

NDf = 45

$p_0 = 1.45949 \pm 0.156283$

$p_1 = -0.732812 \pm 0.124039$

$p_2 = 0.313683 \pm 0.0386788$

$p_3 = -0.0585676 \pm 0.0060948$

$p_4 = 0.00523259 \pm 0.0005146$

$p_5 = -0.000225461 \pm 2.21903e-05$

$p_6 = 3.78568e-06 \pm 3.83644e-07$

For the P = 2.0 bar:

Minimizer is Linear / Migrad

$\chi^2 = 3.24867$e-05

NDf = 3

$p_0 = 3.97411 \pm 0.57577$

$p_1 = -16.5661 \pm 2.28214$

$p_2 = 25.9137 \pm 3.57887$

$p_3 = -19.4437 \pm 2.85496$

$p_4 = 7.79111 \pm 1.2274$

$p_5 = -1.60691 \pm 0.270798$

$p_6 = 0.134115 \pm 0.0240471$

****

Minimizer is Linear / Migrad

$\chi^2 = 1.10761$e-28

NDf = 0

$p_0 = 0.81456 \pm 17.6918$

$p_1 = 0.0246009 \pm 5.65685$

****

Minimizer is Linear / Migrad

$\chi^2 = 0.000730444$

NDf = 45

$p_0 = 1.72378 \pm 0.15977$

$p_1 = -0.764879 \pm 0.126806$

$p_2 = 0.258044 \pm 0.0395417$

$p_3 = -0.0392581 \pm 0.00623077$
$p_4 = 0.00289657 \pm 0.000526081$
$p_5 = -0.000103266 \pm 2.26853e-05$
$p_6 = 1.42871e-06 \pm 3.92203e-07$

For the P = 3.0 bar:

Minimizer is Linear / Migrad
$\chi^2 = 4.97565e\text{-}05$
NDf = 3
$p_0 = 3.39922 \pm 0.712559$
$p_1 = -14.033 \pm 2.82432$
$p_2 = 21.5025 \pm 4.42912$
$p_3 = -15.5659 \pm 3.53323$
$p_4 = 5.97629 \pm 1.51901$
$p_5 = -1.17688 \pm 0.335133$
$p_6 = 0.093652 \pm 0.0297601$

****
Minimizer is Linear / Migrad
$\chi^2 = 5.79936e\text{-}29$
NDf = 0
$p_0 = 1.11405 \pm 17.6918$
$p_1 = -0.0675296 \pm 5.65685$

****
Minimizer is Linear / Migrad
$\chi^2 = 0.000858759$
NDf = 45
$p_0 = 0.529467 \pm 0.173236$
$p_1 = 0.27496 \pm 0.137493$
$p_2 = -0.0904957 \pm 0.0428743$
$p_3 = 0.0178963 \pm 0.00675591$
$p_4 = -0.00192721 \pm 0.00057042$
$p_5 = 9.8829e-05 \pm 2.45973e-05$
$p_6 = -1.90915e-06 \pm 4.25259e-07$

B. Relative gain for different gas pressure and drift chamber lengths.

This table shows a more detailed comparison between the integrated fluxes. Now, the relative percentages are calculated between the spectra at $P = 2.0, 2.0$ bar and the spectra at 1.2 bar for the different chamber sizes, as shown in Table 3. The interpretation of the values is as follows: for instance, in the case of the axion-nucleon spectrum's integrated fluxes for the 6 cm chamber, the relative percentage is 115.50 %. This percentage represents the integrated flux of the spectrum at 3 bar divided by the corresponding flux at 1.2 bar, multiplied by 100. Essentially, this indicates that the integral of the flux at 3 bar is 1.15 times higher than the flux at 1.2 bar. The rest of the values follow the same rule. There can also be noted that all the percentages refer to an increment or gain, not to a decrease in the flux.

P (bar)	**ABC**	**Primakoff**	**aN**
	3 cm drift d.	vs 3 cm drift d.	
2.0	8.00 %	10.80 %	66.02 %
3.0	11.78%	16.09 %	140.21 %
	6 cm drift d.	vs 6 cm drift d.	
2.0	2.72 %	4.10 %	157.07 %
3.0	3.85 %	5.60 %	115.50 %
	6 cm drift d.	vs 3 cm drift d.	
1.2	9.96 %	13.37 %	195.48 %
2.0	12.95 %	18.01 %	287.20 %
3.0	14.19 %	19.71 %	321.24 %

Table 3: Relative increments in % of the integrated values of convoluted spectra using 1.2 bar total flux as reference. Top: fluxes at P = 2, 3 bar in 3cm chamber vs P = 1.2 bar in 3cm chamber; middle: fluxes at P = 2, 3 bar in 6cm chamber vs P = 1.2 bar in 6 cm chamber; and bottom:fluxes at P = 1.2, 2, 3 bar in 6cm chamber vs P = 1.2 bar in 3cm chamber.

C. Axion-to-photon conversion probability.

In order to detect solar axions in a laboratory experiment, helioscopes are designed to employ magnetic fields to convert axions into X-ray photons via the inverse Primakoff effect see Fig. 1. In this interaction, the virtual photon is provided by the transverse component of the magnetic field. What is more, the conversion process works in a manner analogous to neutrino oscillations [1]. The photon has spin one and axions are spin zero particles, but the mixing is possible in an external, transverse magnetic or electric field that makes possible the matching of the missing quantum numbers.

Knowing the amplitude of the photon field component parallel to the magnetic field (B) and the amplitude of the axion field, the wave equation for axions propagating perpendicular

to this magnetic field can be determined. With it, the conversion probability of axions into photons at a length $z = L$ within the helioscope can be obtained [1, 51]:

$$P_{a\to\gamma} = \left(\frac{Bg_{a\gamma\gamma}}{2}\right)^2 \frac{1}{q^2 + \Gamma^2/4} \left[1 + e^{-\Gamma L} - 2e^{-\Gamma L/2} cos(qL)\right], \tag{10}$$

where Γ is the damping coefficient or inverse absorption length of X-rays and q is the absolute momentum transfer between the real photon in the medium and the axion, defined as follows:

$$q = \left|\frac{m_\gamma^2 - m_a^2}{2E_a}\right|, \tag{11}$$

where E_a is the energy of the axion,m_γ is the effective photon mass in the gas, and m_a is the axion mass.